

Southern Methodist University

SMU Scholar

---

Mechanical Engineering Research Theses and  
Dissertations

Mechanical Engineering

---

Spring 5-13-2023

## Photonic Sensors Based on Integrated Ring Resonators

Jaime Da Silva

*Southern Methodist University*, [odasilva@smu.edu](mailto:odasilva@smu.edu)

Follow this and additional works at: [https://scholar.smu.edu/engineering\\_mechanical\\_etds](https://scholar.smu.edu/engineering_mechanical_etds)



Part of the [Acoustics, Dynamics, and Controls Commons](#), [Dynamical Systems Commons](#), and the [Optics Commons](#)

---

### Recommended Citation

Da Silva, Jaime, "Photonic Sensors Based on Integrated Ring Resonators" (2023). *Mechanical Engineering Research Theses and Dissertations*. 52.

[https://scholar.smu.edu/engineering\\_mechanical\\_etds/52](https://scholar.smu.edu/engineering_mechanical_etds/52)

This Dissertation is brought to you for free and open access by the Mechanical Engineering at SMU Scholar. It has been accepted for inclusion in Mechanical Engineering Research Theses and Dissertations by an authorized administrator of SMU Scholar. For more information, please visit <http://digitalrepository.smu.edu>.

PHOTONIC SENSORS BASED ON  
INTEGRATED RING RESONATORS

Approved by:

---

Dr. M. Volkan Ötügen  
Professor of Mechanical Engineering

---

Dr. Edmond Richer  
Professor of Mechanical Engineering

---

Dr. Yildirim Hurmuzlu  
Professor of Mechanical Engineering

---

Dr. Duncan MacFarlane  
Professor of Electrical and Computer  
Engineering

---

Dr. Dominique Fourquette  
Senior Remote Sensing Engineer  
Perikin Enterprises

---

Dr. Bruce Gnade  
Professor of Electrical and Computer  
Engineering

PHOTONIC SENSORS BASED ON  
INTEGRATED RING RESONATORS

A Dissertation Presented to the Graduate Faculty of the

Lyle School of Engineering

Southern Methodist University

in

Partial Fulfillment of the Requirements

for the degree of

Doctor of Philosophy

with a

Major in Mechanical Engineering

by

Jaime Ottoniel Junqueira da Silva

B.S., Mathematics, Southern Methodist University

B.S., Mechanical Engineering, Southern Methodist University

M.S., Mechanical Engineering, Southern Methodist University

May 13, 2023

Copyright (2023)

Jaime Ottoniel Junqueira da Silva

All Rights Reserved

## ACKNOWLEDGMENTS

First, I would like to thank my advisor, Dr. M. Volkan Ötügen. To say that his help, patience, and guidance were crucial to the research and the development of this work would be an understatement. I could never thank him enough for allowing me to join his lab and participate in challenging and innovative research projects. He consistently steered me in the right direction as I developed from an undergraduate student to a doctoral candidate and a scientist. I will always carry with me the countless lessons he taught me as my advisor and mentor.

I would also like to thank my thesis committee: Dr. Yildirim Hurmuzlu, Dr. Edmond Richer, Dr. Duncan MacFarlane, Dr. Dominique Fourquette, and Dr. Bruce Gnade, for their participation and input, which improved the quality of this work.

Dr. Fourquette has been one of the biggest influences in my research these past six years. Her research initiative gave me the support needed to develop this dissertation's chapters 2 and 3. I will always cherish our discussions as we ventured into the intellectual unknown and returned with amazing concepts and ideas. I look forward to continuing to collaborate with her and learning from her experience and brilliant mind.

Dr. Gnade is unofficially a co-advisor in this dissertation. He has been a great mentor throughout my Ph.D. He welcomed me into his team and pushed me to work in an area outside of my comfort zone and expand my knowledge base. He has also supported my initiatives while objectively assessing their potential. I am excited to continue working with him in the next chapter of my career.

As part of the Dynamics and Controls family, I would also like to thank my instructors: Dr. Richer, Dr. Hurmuzlu, and Dr. Borzova. Dr. Richer has been one of the most notable instructors in my academic journey. He was always available to help me whenever I struggled

with concepts in Dynamics and Controls. His help in my preparation for the Qualifiers Exams was crucial to my success. Dr. Hurmuzlu's recommendation was critical for me to join the Accelerated Path program and start graduate school.

I would also like to thank Dr. MacFarlane for exchanging ideas with me regarding optical resonators. He provided me with the Silicon resonators used to carry out the experimental work presented in Chapter 4. His kindness was vital to demonstrating the self-referencing concept, thus, completing this work.

Additionally, I would like to thank the members of the Department of Mechanical Engineering at SMU's Lyle School of Engineering; the department coordinators and executive assistants: Susan Bailey, Elizabeth Wright, Rebecca Tiemann, Stephanie Murray, and Sarah Laue; the folks at the machine shop: Mr. Necdet Yildirimer and Mr. Kenneth Sangston. I would also like to express my gratitude to the people in the Earth Science department who helped promote my research: Dr. Louis Jacobs, Mrs. Diana Vineyard, and Mrs. Maria Richards.

To my friend and colleague, Dr. Elie Salameh, it was a great experience sharing the MicroSensor Lab with you. Our conversations and exchange of ideas were memorable aspects of my Ph.D. I am thankful for your patience whenever I bothered you with a new idea or concept. I could not have asked for a more disciplined, systematic, and knowledgeable lab mate. Mr. Alejandro Bolivar has been a very supportive friend and colleague. While I worked on this dissertation, his continuous checkups were meaningful to me, and he has my gratitude.

Thank you very much to my family and friends who believed in me. To Mr. Helmer de Sousa, my best friend, brother, and father of my godson, I appreciate you always being there for me when needed and being an exemplary person for me and others. To Ms. Olivia Asenime, you were one of the first people to push me to join graduate school and support me in any way you could, and for that, you have my eternal gratitude. To my Angolan Dallas crew (NKS), thank you for all the fantastic moments we shared along this journey. I will always cherish how we rallied as a small community to support each other in times of need.

I am also thankful for my late father, Mr. Jaime da Silva, who pushed and inspired me to do my best. I would not be here if not for all that my father did for me. To my godfather, Mr. Baptista Sumbe, thank you for making it possible for me to pursue a bachelor's degree in the U.S., which has become a defining moment in my personal, academic, and professional life. This work is proof of it. To Mr. Augusto Zeferino, my uncle, who I had the pleasure to call father over the course of my life, thank you for coming to my aid whenever required. You have provided me with guidance and emotional support for many years, especially during some of the most challenging periods of my life. I am grateful for Mr. Francisco Carvalho's encouragement when I doubted myself. You called me Dr. even when I started my M.S. program, and your confidence made a big difference in this journey. To Mr. Manuel da Silva Neto, thank you for all the great conversations and knowledge you shared with me. At the beginning of this journey, you dared me to believe and challenge for dreams beyond what I thought myself capable of.

Thank you to the special women in my life – my sisters and mother. Mrs. Florinda Azevedo, Mrs. Suely Ulombe, and Mrs. Analgiza Carvalho, you guys have always been there for me and had to accept my absence from our lovely home. I relied on your love to push through when my strength failed me. I hope this milestone is an acceptable excuse for my absence in your life.

Finally, I would like to acknowledge the most special person in my life, my mother, Ms. Catarina Aniceta Junqueira. I cannot find the words to express how grateful and blessed I am for having you as my mother. Your unconditional love and unwavering support throughout this journey were vital to its success. You accepted that your son, at 13 years of age, moved across the country to follow his path. This achievement is as mine as it is yours. I am all that I am today, thanks to you.

Junqueira da Silva, Jaime Ottoniel B.S., Mathematics, Southern Methodist University  
B.S., Mechanical Engineering, Southern Methodist University  
M.S., Mechanical Engineering, Southern Methodist University

Photonic Sensors Based on  
Integrated Ring Resonators

Advisor: Dr. M. Volkan Ötügen

Doctor of Philosophy degree conferred May 13, 2023

Dissertation completed April 10, 2023

This thesis investigates the application of integrated ring resonators to different sensing applications. The sensors proposed here rely on the principle of optical whispering gallery mode (WGM) resonance shifts of the resonators. Three distinct sensing applications are investigated to demonstrate the concept: a photonic seismometer, an evanescent field sensor, and a zero-drift Doppler velocimeter. These concepts can be helpful to develop lightweight, compact, and highly sensitive sensors. Successful implementation of these sensors could potentially address sensing requirements for both space and Earth-bound applications. The feasibility of this class of sensors is assessed for seismic, proximity, and vibrational measurements.



## TABLE OF CONTENTS

LIST OF FIGURES .....	vii
LIST OF SYMBOLS .....	xi
CHAPTER	
1. INTRODUCTION .....	1
1.1. Background and Motivation .....	2
1.2. Optical Seismometers .....	7
1.3. WGM Principle .....	9
1.4. Previous WGM Sensors .....	11
2. Photonic Seismometer .....	13
2.1. Seismometer Concept .....	14
2.2. Sensor System .....	17
2.2.1. Signal Processing .....	18
2.3. Results .....	20
2.3.1. Static Characterization .....	20
2.3.2. Harmonic Excitation .....	23
2.3.3. Free Vibration .....	25
2.3.4. Resolution and Dynamic Range .....	27
2.3.5. Damping .....	27
2.3.6. Computations on a Raspberry Pi 4 .....	29
2.3.7. Thin SiO <sub>2</sub> -Si-SiO <sub>2</sub> Beam .....	29
2.3.8. Nonlinearity Considerations .....	31
3. Evanescent Field-Based Sensing .....	33
3.1. Sensor Concept .....	33
3.2. Numerical Analysis .....	34

3.3. Experimental Setup and Results .....	36
3.3.1. Sphere Resonator .....	38
3.3.2. Ring Resonator .....	40
3.4. Future Considerations .....	45
4. Self-Referencing WGM-based Doppler Sensor .....	48
4.1. Sensor Concept .....	49
4.2. Optoelectronic Configuration .....	51
4.3. Measurement Technique .....	53
4.4. Experimental Setup .....	53
4.5. Results .....	56
4.6. Future Considerations .....	59
5. Conclusion .....	60
BIBLIOGRAPHY .....	65

## LIST OF FIGURES

Figure		Page
1.1	Payload of the (a) EASEP [52] and (b) ASLEP science missions [36].....	3
1.2	Rendering of SEIS-VBB pendulum (a) and its components: (b) fixed part; (c) moving part; (d) spring; (e) pivot; (f) feedback electromagnetic actuator; (g) balancing mechanism; (h) thermal compensation device mechanism; (i) differential capacity sensor. Courtesy of SEIS-Insight website.....	5
1.3	Assembly of the microsphere-based optical seismometer described in US patent US8743372.....	9
1.4	Snapshot of a simulation of a waveguide-coupled ring resonator undergoing WGM excitation and an idealized transmission spectrum showing a WGM dip and mode shift.....	11
2.1	3D rendering of the sensing element (a) and top view photograph of the assembled seismometer (b).....	15
2.2	Schematic of the sensor system. ....	18
2.3	Demonstration of (top) DD, (center) CC, and (bottom) LF signal processing algorithms for automatic WGM shift measurement. ....	19
2.4	Apparatus employed for the determination of static force sensitivity (left) and geometry of 3D computational model (right).....	21
2.5	Shift of optical resonance due to force applied by linear spring (a), and measured WGM shift as function of the applied force (b).....	21
2.6	Schematic of the shake table experiment used for harmonic base excitation .....	23
2.7	(a) WGM shift (circles) and acceleration of table (solid line); (b) Phase corrected plot of WGM vs measured acceleration. The solid line is the line fit. The small deviation of the experimental data from the line is attributed to the asymmetry in the clamping mechanism. ....	24

2.8	(a) Free vibration of the seismometer; (b) Ring down fitting of equation (2.14) (solid line) and experimental values (circles); (c) Peak normalized frequency response from experiment (circles), equation (2.15) with estimated parameters from (2.14) (solid line), and analytical $Q_m$ (dashed line). The response of the prototype photonic seismometer agrees with the spring-mass-damper model and is linear up to approximately 40 Hz	26
2.9	Normalized amplitude of sensor response before (blue) and after damping (red). The solid lines are fit of Eq. (2.14). The inclusion of a PDMS block between the proof-mass and the chip carrier introduces additional damping into the sensor. ....	28
2.10	(a) Cross-section of a representative thin beam sample; (b) Schematic of apparatus used to measure the response of the thin plate. ....	30
2.11	Amplitude spectrum of thin cantilever vibration under impulse excitation. The solid line is the fit of Eq. (2.15). For the thin plate $\omega_n = 60$ Hz with a proof-mass of 0.25 g. For comparison, the thick beam required a 70-g proof-mass to reach $\omega_n = 80$ Hz. ....	31
3.1	Geometry for the computational model for sphere resonator (top) and ring resonator (bottom). The left figures show a 3D rendering of the geometry under consideration. The center figures illustrate the top view of the geometry and the selection of azimuthal angles resulting in the right figures. The variation of the azimuthal angle leads to different cross-sections (varying gap between resonator and perturber). ....	35
3.2	Computational analysis of the optical modes of a sphere (left) and an integrated ring (right) resonator. Resonator geometry and corresponding refractive indices (a,d); transverse electric field distribution (b,e); radial distribution of transverse electric field and evanescent tail (in red) (c,f).	37
3.3	Photograph of sphere resonator and perturber: (a) top view of the sphere resonator coupled to tapered fiber on the left and a perturber on the right side; (b) side view and close up of sphere-perturber interaction region.	38
3.4	Experimental results for the perturbation of the spherical resonator. The inset shows the spectrum of the sphere for two different positions of the perturber. ....	39
3.5	(a) WGM shift with azimuthal angle for $d = 50$ nm. (b) WGM shift as a function of gap between the resonator and perturber. Each value in (b) corresponds to an integral of the curve in (a), using Eq. (3.3), for different gap values. ....	40

3.6	Cutaway representation of the on-chip ring resonator and perturber (not drawn to scale). Coordinates $r$ and $z$ are measured from the center of ring and chip's top surface. ....	41
3.7	Normalized electric field magnitude: (a) Radial distribution along chip's surface; (b) Surface normal distribution. Since there is an evanescent tail extending past the chip's top surface, the modes of the ring resonator can be perturbed. ....	42
3.8	Photograph of the perturber and the ring resonator (top view). ....	42
3.9	WGM shift versus perturber position. The computational curve is obtained using eq. (3.3) and the process described in fig. 3.5.....	43
3.10	Photograph of magnetic field detection setup. The perturber sits on the top surface of chip. The solenoid generates a magnetic field that pulls the ferromagnet, causing the perturber to move across the evanescent field of the ring resonator. ....	44
3.11	WGM shift versus magnetic field. (a) Single realization - each data point corresponds to one laser scan at a rate of 400 Hz. (b) Averaged measurement for 20 realizations with standard deviation for each magnetic field value shown as error bars. ....	45
3.12	Example of on-chip ring resonator with a built-in perturber (cantilever beam).....	46
3.13	Mode shift and Q-factor of ring resonator as the perturber interacts with the evanescent tail. The Q-factor is modulated by the interaction between the perturber and ring resonator.....	47
4.1	Schematic representation of Doppler effect for a uniformly moving surface. ....	49
4.2	Optical wave vectors for a retro-reflective surface. ....	50
4.3	Opto-electronic configuration of the self-referencing WGM-based Doppler sensor. ....	52
4.4	Illustration of measurement technique. The dashed lines correspond to the wavelength of the input light before (blue) and after (red) a Doppler shift is introduced. The solid lines are the spectrum of a ring resonator measured by the original laser light (blue) and the Doppler shifted light (red). ....	54
4.5	Top (left) and side (right) views of experimental apparatus. In the side view a red-light alignment laser is used to indicate the focal point of the lens. ....	55

4.6	Characterization of resonances in the two propagation directions: (orange) from disk (counter-clockwise rotation) and (blue) from laser (clockwise rotation) - see Fig. 4.3. The solid lines are the Lorentzian fitting for each WGM. ....	57
4.7	Sensing resonance for two different rotational speeds. The x-axis is offset by the location of the reference resonance. ....	57
4.8	Measured Doppler shift and best fit line as a function of angular velocity .....	58

## LIST OF SYMBOLS

$A$	Proportionality Constant: Proof Mass Displacement to Mode Shift
$c$	Speed of Light in Vacuum
$C_p$	Specific Heat
$E$	Young's Modulus
$\vec{E}$	Electric Field Vector
$h$	Distance from Neutral Axis
$H$	Thickness of Beam
$I$	Area Moment of Inertia
$P$	Load Applied to Free End of Cantilever
$\vec{k}$	Wave Number
$L$	Length of Beam
$L_i$	Perimeter of Resonator Before Deformation
$L_f$	Perimeter of Resonator After Deformation
$l$	Mode Number
$n$	Effective Refractive Index
$Q$	Optical Quality Factor $Q = \lambda/\delta\lambda$
$Q_{air}$	Mechanical Quality Factor Associated with Viscous Damping in Air
$Q_{bulk}$	Mechanical Quality Factor Associated with Internal Material Friction
$Q_{clamp}$	Mechanical Quality Factor Due to Beam-Clamp Interaction
$Q_m$	Mechanical Quality Factor
$Q_{other}$	Contribution from Other Loss Mechanism to the Mechanical Quality Factor
$Q_{TE}$	Quality Factor Due to Thermoelastic Losses

$R$	Resonator Radius
$r_o$	Average Resonator Radius
$y_b$	Displacement of the Base
$y_m$	Displacement of Proof Mass
$y_o$	Amplitude of Proof-Mass Displacement in Time Domain
$V$	Laser Driving Voltage
$v$	Magnitude of Velocity Vector
$\vec{V}$	Velocity Vector of Target's Motion in Doppler Shift Sensor
$W$	Width of Beam
$w(x)$	Transverse Displacement of Cantilever Beam
$\alpha$	Angle Between Optical Axis and Target's Velocity Vector
$\alpha_T$	Linear Thermal Expansion Coefficient
$\epsilon_{xx}$	Longitudinal Strain
$\Delta\lambda$	Shift of Resonant Wavelength
$\delta\lambda$	WGM Resonance Full Width at Half Max
$\Delta\lambda_D$	Doppler Shift
$\Delta\phi_o$	Range of Azimuthal Angle Over Which Resonator and Perturber Interact
$\kappa_{th}$	Thermal Conductivity
$\lambda$	Wavelength
$\lambda_r$	Resonant Wavelength
$\lambda_{res}(\phi)$	Resonant Wavelength for Azimuthally Varying Resonator's Cross-Section
$\phi$	Azimuthal Angle of Resonator's Cross-Section
$\omega$	Driving Frequency of the Base
$\omega_n$	Natural Frequency
$\omega_d$	Damped Natural Frequency
$\theta_o$	Phase of of Proof-Mass Displacement in Time Domain
$\rho$	Density



This work is dedicated to my grandparents, Mr. Antonio Junqueira and Mrs. Antonia Namahuma, and Mr. Carlos da Silva and Mrs. Florinda Silveira. Throughout this journey, I've felt closer to them and relied on the strength I inherited from them through my parents.

## Chapter 1

### INTRODUCTION

This work explores the application of whispering gallery mode (WGM) photonic sensors based on integrated ring resonators with specific emphasis on seismometry. The photonic seismometer presented here aims to address the need for compact, robust, and low noise (including electromagnetic interference) seismic sensors for both Earth applications and planetary exploration. Additionally, the dissertation presents the concept of a versatile evanescent field perturbation-based sensor and a self-referencing speed sensor based on the detection of Doppler shifts. The evanescent field perturbation sensor concept demonstrates the potential of using WGM resonators to measure mechanical parameters such as displacement and acceleration as well as to detect electric and magnetic fields. The self-referencing sensor study proposes a WGM flow velocity and surface vibration concept that uses a single optical ring resonator for both measurement and reference for automatic drift correction. In general, the three concepts discussed in this dissertation demonstrate the potential of optical ring resonator-based sensors for both Earth applications and space exploration.

Planetary seismology is one of the fields that would benefit from the development of compact photonic sensors. Studying the composition and history of terrestrial planets requires measuring naturally occurring or induced seismicity with devices installed on their surface. Planetary missions use seismic sensors that are specifically developed or modified for the environment in which they will operate. So far, seismic sensors used in planetary missions are mainly based on traditional electromechanical systems that, despite their performance benefits, are often challenging to miniaturize - an essential factor when considering the constraints of space exploration. Electromechanical seismometers are also susceptible to variations in ambient conditions (i.e., temperature and pressure) and electromagnetic interference. Current planetary seismic sensors require secondary instruments and compensation

systems to ensure reliable operation. The 1969 Apollo Lunar and the 2018 InSight Mars missions, along with their spectacular successes, provide valuable information on extraterrestrial seismometers' limitations and challenges [36,38].

### **1.1. Background and Motivation**

The National Aeronautics and Space Administration's (NASA) Apollo Lunar Surface Experiment Package (ALSEP, 1969-1977) employed seismometers to study the interior structure and composition of the Moon. The first seismometer successfully deployed in space was part of Apollo 11's Early Apollo Surface Experiments Package (EASEP) [37]. This preliminary sensor package included a triaxial long-period (LP) and a vertical short-period (SP) seismometer. These devices provided an initial assessment of the challenges for Lunar seismometers. They measured the impact of meteorites and moonquakes and relayed the data back to stations on Earth. The solar panels powered the sensor package and could only operate during Lunar days. One of the main challenges for these early seismometers was to survive the cold Lunar nights when the temperature drop could damage the sensors. Although the sensor package used thermal units to control the temperature, the seismometers remained operational for 21 days before they stopped responding, likely due to overheating [36]. Subsequent missions improved on the initial seismometer design through the valuable lessons from EASEP.

The ALSEP was part of the subsequent Apollo missions (12-17) and had a much larger scientific payload than the EASEP as shown in Fig. 1.1 [36]. The Lunar Passive Experiment (PSE) included a triaxial LP and a vertical SP geophone that could withstand the harsh Moon conditions thanks to an improved support system. In addition to the PSE, the ALSEP also realized an Active Seismic Experiment (ASE) that used explosives to generate seismic waves. The data from ALSEP provided valuable insight into the Moon's induced and passive seismic characteristics. Thanks to the success of ALSEP, seismologists could determine the composition and structure of the Moon's subsurface down to approximately 50 km. The seismometers remained operational until 1977, when the ground station deactivated them.

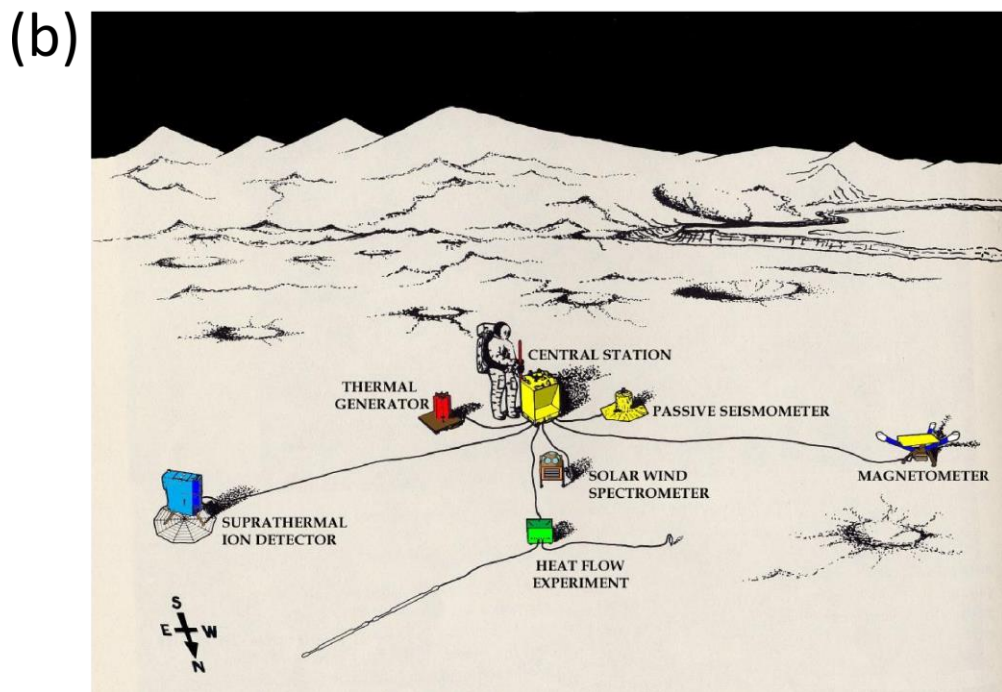
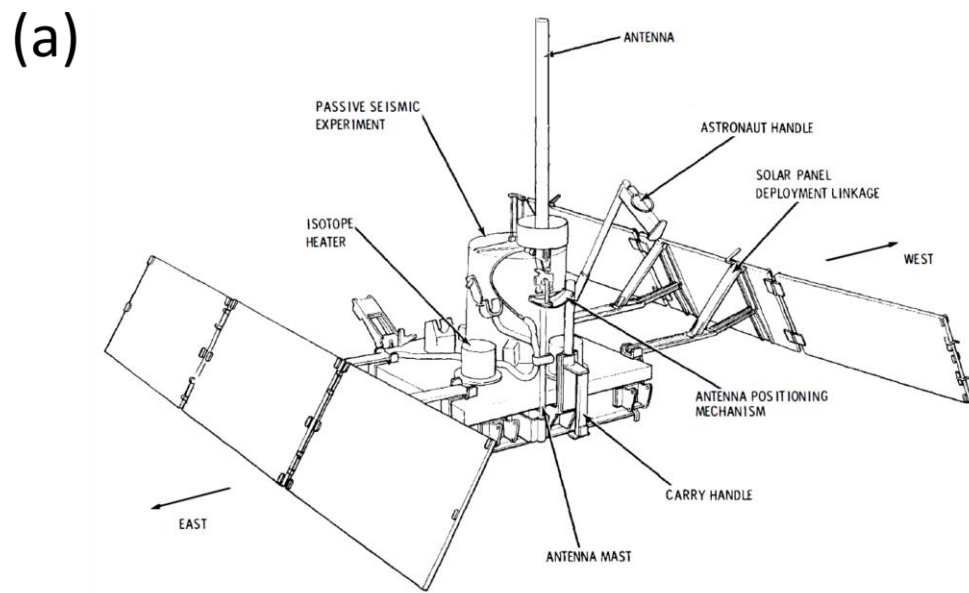


Figure 1.1: Payload of the (a) EASEP [52] and (b) ASLEP science missions [36]

The seismometers deployed in the Apollo missions are traditional electromechanical geophones. These devices convert the motion (velocity) of a proof mass into electrical current using a spring-mass and coil-magnet assembly, with an amplifier that increases the intensity of the signal to measurable levels. Despite their proven track record, geophones are susceptible to temperature variations that can change the overall sensor assembly's mechanical, magnetic, and electric characteristics. In particular, the performance of the LP-ALSEP geophones had to be assisted by a temperature sensor to correct the influence of temperature on the recorded seismic signals. Furthermore, as demonstrated by PSEP, the geophones' temperature had to be controlled to prevent the components from being damaged due to extreme temperatures. The ALSEP required a thermal unit that consumed power to control the sensor package's temperature. In contrast, the most recent planetary mission (InSight) employs a different approach to overcome the wide variations in temperature and other issues related to ambient conditions.

NASA's InSight mission deployed the Seismic Experiment for Interior Structures (SEIS) sensor package to study the composition of Mars. InSight's primary device is a very broadband (VBB) triaxial seismometer that monitors Martian seismic activity. SEIS-VBB is considered to be the most advanced seismometer in planetary exploration to date and provides excellent data on the seismic activity of Mars [9]. The SEIS-VBB is a sophisticated sensing system that relies on complementary devices to achieve high performance (see Fig. 1.2). This seismometer uses an inverted pendulum (one for each axis) alongside a differential capacitive sensor (DCS) that measures the pendulum's displacement based on a proximity effect.

The SEIS-VBB includes a Thermal Compensation Device Mechanism (TCDM) that offsets the deviation of the natural frequency of the pendulum assembly due to temperature variations. Additionally, the system has multiple layers of thermal insulation, including an evacuated chamber that houses the VBB and a wind and thermal shield (WTS) that protects the seismometer from wind gusts. The SEIS-VBB is susceptible to electromagnetic interference mainly due to the leaf spring, whose mechanical properties change with exposure to

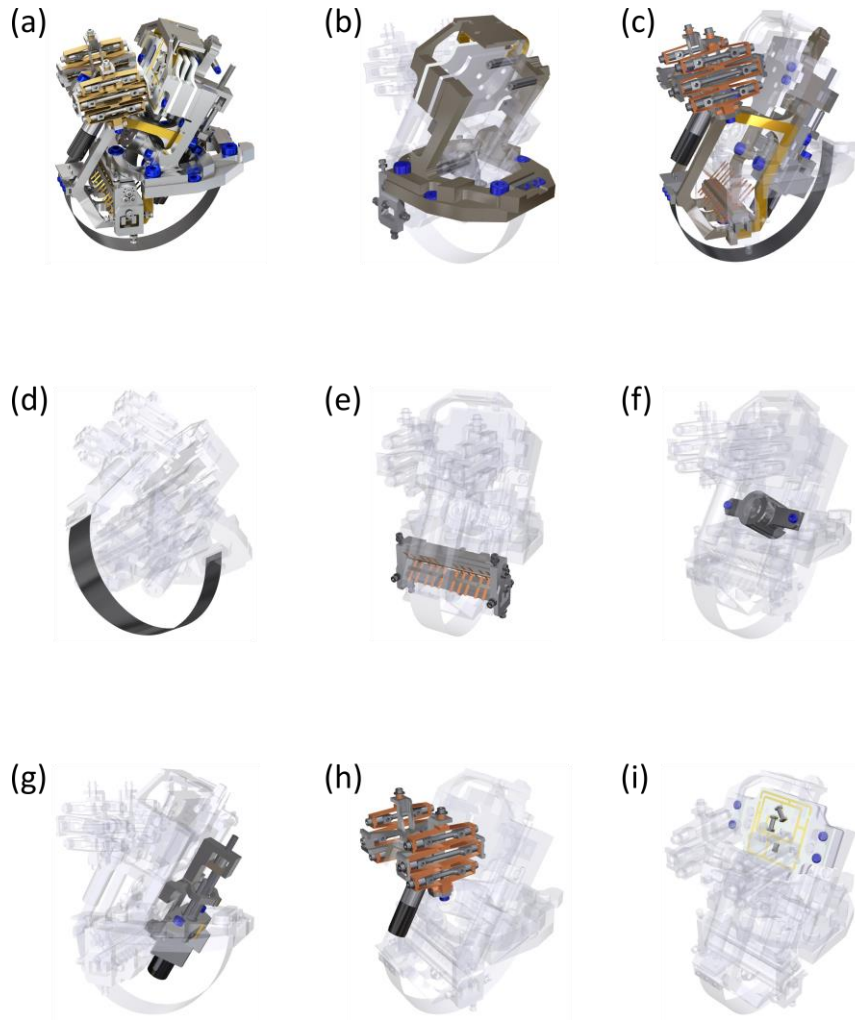


Figure 1.2: Rendering of SEIS-VBB pendulum (a) and its components: (b) fixed part; (c) moving part; (d) spring; (e) pivot; (f) feedback electromagnetic actuator; (g) balancing mechanism; (h) thermal compensation device mechanism; (i) differential capacity sensor. Courtesy of SEIS-Insight website.

magnetic fields [38]. The need for compensation and auxiliary sensors for the proper functioning of the SEIS-VBB highlight this type of sensor's limitations for missions on planets further away from Earth and with more extreme and challenging environments (for example, Jupiter's moon Europa, which has received significant interest in recent years with orbital missions and a planned lander).

The SEIS also contains a compact short-period microfabricated silicon-based sensor dedicated to detecting and measuring higher frequency seismic events in the 0.1-40 Hz band [38]. The SEIS-SP is an active MEMS device that relies on a periodic linear capacitive array of transducers that measures the position of a proof-mass. Three individual sensor packages are employed to achieve a 3D seismometer. One of the main benefits of the silicon-based SEIS-SP is that it is not susceptible to electromagnetic interference. The SEIS-SP provides some redundancy for the SEIS-VBB and monitors events outside its bandwidth. This sensor demonstrates one of the advantages of using silicon (and similar) materials for applications where exposure to radiation can affect the functioning of the sensor.

The employment of the SEIS-SP suggests the need for compact and rugged devices in planetary seismology. Additionally, the sensitivity to variations in ambient conditions (mainly pressure and temperature), as observed in both the VBB and the SP instruments [8], is an issue that a different type of sensor perhaps could address. While space missions would be the primary benefactor of developing compact and robust seismometers, Earth-bound applications, such as remote sensing, could also benefit. An integrated optical micro-seismometer would address the requirements of both Earth applications and planetary missions.

All the sensors discussed so far are of the electronic type. One of the drawbacks of electromechanical seismometers is that they cannot be placed very far from the required electronics (e.g., power supply, amplifier, filters). For example, the sensors are installed near the landers in the Apollo and InSight missions. In contrast, optical seismometers need not be placed near the attending electronics since they can rely on low-loss optical fibers as either the sensing element (e.g., distributed acoustic sensing) or a communication line to the

sensing element. Furthermore, optical sensors are potentially more resistant to high-energy particles that often affect electronics exposed to strong EM radiation [21].

It is essential to consider optical sensors that could address some of the challenges in planetary seismology. Optical seismometers present an alternative to their electromechanical counterparts since they operate on different principles and can be rendered immune to most of the disturbances that affect electromechanical seismometers. Furthermore, photonic sensing platforms can integrate miniature sensors to assist the functioning of designated sensors and measure other auxiliary parameters.

## **1.2. Optical Seismometers**

On Earth, most modern seismometers consist of spring-mass active devices employing an electromagnetic feedback force unit that prevents the movement of the proof-mass [58]. The magnitude of the force required to maintain the mass at rest determines the ground motion. Thanks to the closed-loop feedback, the response of the seismometer can be configured to cover a designated band and reach a higher sensitivity. However, the addition of circuitry introduces both electronic noise and heat generation due to electric power dissipation. Traditional passive seismometers, such as geophones, also require amplifiers to increase the intensity of the generated electrical signal. Optical seismometers present an attractive alternative to electromechanical seismometers as they eliminate the need for electronics near the sensing element. While there is a variety of laser-based seismometers, interferometric optical seismic sensors present a particularly desirable alternative to their electromechanical counterparts since they employ a different operating principle, rendering them inherently resistant to the same type of undesirable perturbations.

Various groups have presented several interferometric optical seismometers for applications on Earth. An optical seismic sensor was developed using an open-loop vertical seismometer based on a Michaelson interferometer [62]. This sensor relies on the displacement of a mirror attached to the leaf-spring mechanism of a modified STS1 seismometer [57]. The *i*STS1 (*i* corresponding to interferometric) seismometer responds to acceleration. It was



deployed to measure ground motion in the Black Forest Observatory [5]. The Michaelson interferometric technique was also applied to develop a 3-component borehole seismometer. This sensor was deployed in the Albuquerque Seismological Laboratory and used to measure an earthquake [61]. The outputs of the iSTS1 show good agreement with more established instruments, such as STS1 [62], STS2 [5], and KS-54000 [61] seismometers.

Motivated by the promising preliminary work of [63], a group at the Institut de Physique du Globe de Paris developed a Fabry-Pérot-based optical geophone as part of the Laser Interferometry for Earth Strain (LINES) project [6]. This device consists of a modified short-period geophone (2 Hz) with a mirror attached to its mobile mass. An optical fiber transmits a light beam that is reflected by the mirror and injected back into the fiber to generate an interferometric signal. The ground motion is determined from the phase difference of two signals, obtained by demodulating the interferometric signal using a dedicated signal processing circuit. Through this project, a 3D LINES geophone was successfully employed for remote measurement of ground motion (velocity) on the seafloor. This sensor proves to be low noise and highly sensitive, capable of resolving velocities as small as 12 pm/s (noise floor) with a dynamic range of 28 bits (based on 2 mm/s velocity cutoff). Although the LINES seismometer offers good performance, it requires the protection of the geophone from corrosion of its metallic components due to atmospheric humidity. Additionally, the reliance on a long stretch of optical fiber to generate interference makes the approach susceptible to external conditions. As presented in this work, a more direct interferometric measurement approach may be achieved using a resonant optical cavity, such as a WGM.

WGM sensors based on optical mode shifts are shown to be effective for seismic applications such as that presented in US patent no. 8743372 [14] (Fig. 1.3). This approach relies on the resonant frequency shift of the optical modes of a fiber-coupled dielectric microsphere (200-1500  $\mu\text{m}$  in diameter). Unlike the previously discussed interferometric sensors, resonance is generated in a circular geometry optical cavity. These WGM resonances are observed as sharp dips in the transmission spectrum of the fiber coupled to the resonator, as most of the optical energy is contained in the resonator. A leaf-spring-mass modifies

the shape of the microsphere, leading to a resonant optical frequency (WGM) shift. The ground motion (acceleration) is determined by tracking the location of the WGMs. This device is compact, lightweight, and low-power, capable of resolving acceleration in the order of 1 nano-g with a dynamic range of 10 bits [15]. Despite its successful implementation, the sensor is limited by the mechanical weakness of the fiber-to-resonator coupling, which impedes its potential use in the field. The current seismometer proposed in Section 2 is the next-generation implementation of the one presented in US8743372. The core optical element is an on-chip waveguide-coupled ring resonator (instead of a fiber-coupled sphere resonator). Its monolithic design allows for a rugged sensor suitable for field deployment.

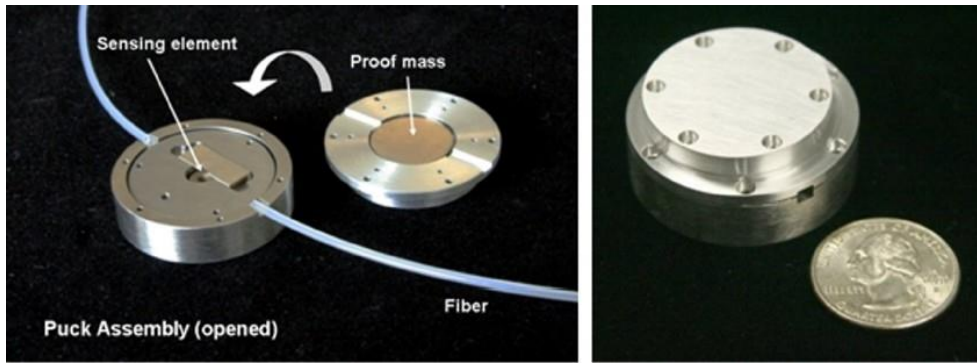


Figure 1.3: Assembly of the microsphere-based optical seismometer described in US patent US8743372

Optical seismometers offer various benefits over their electromagnetic counterparts. Since the sensing element consists of dielectric materials, there is a significant reduction in the influence of electromagnetic interference. Optical seismometers connected by low-loss fiber networks can also be deployed at great distances from optoelectronic processing systems [6]. The all-optical fiber input/output connections allow for the multiplexing of this class of sensors into seismometer networks. Lastly, the versatility of WGM sensing allows for the employment of other optical reference sensors designed to compensate for the variations in ambient conditions (e.g., temperature/pressure) that can affect the output signal [50].

### 1.3. WGM Principle

The concept of WGM was first mathematically formulated by Lord Rayleigh in the 19th century to describe the frequency-selective propagation of sound waves along the concave surface of a solid wall [47]. Since then, the same phenomenon has been observed for electromagnetic waves on curved optical cavities, often referred to as optical WGM. For a circular cavity, the geometric formulation of WGM yields an approximate resonant condition given by:

$$2\pi Rn = l\lambda_r, \quad (1.1)$$

where  $R$ ,  $l$ ,  $n$ , and  $\lambda_r$  are the radius of the resonator, polar mode number (integer), the effective refractive index of the optical mode, and resonating wavelength, respectively. This expression is only a first-order approximation of the resonant condition but is sufficiently accurate for  $R \gg \lambda$  [24].

Equation (1.1) indicates that the resonance depends on  $R$  and  $n$ , so changes in the morphology of the resonator lead to a shift of the resonant wavelength. This dependence is expressed as [26]:

$$\frac{\Delta\lambda}{\lambda} = \frac{\Delta R}{R} + \frac{\Delta n}{n}. \quad (1.2)$$

Multiple strain-based WGM sensors are demonstrated in the literature for the measurement of quantities such as pressure [28], force [26], temperature [16], and acceleration [31], to name a few. The versatility of this class of sensors makes them attractive for a wide range of applications. In the current application, the contribution to the WGM shift from the effective refractive index (photoelastic effect) is negligible as the effect of the mechanical strain ( $\Delta R/R$ ) dominates the mode shift [24].

When light from a tunable laser is injected into a waveguide that is evanescently coupled to a ring resonator, the WGMs are observed as sharp dips in the transmission spectrum, as computationally demonstrated in Fig. 1.4. The mode shift ( $\Delta\lambda$ ) and the resonance linewidth ( $\delta\lambda$ ) are obtained by observing the transmission spectrum. The optical quality factor, defined as

$$Q = \frac{\lambda}{\delta\lambda}, \quad (1.3)$$

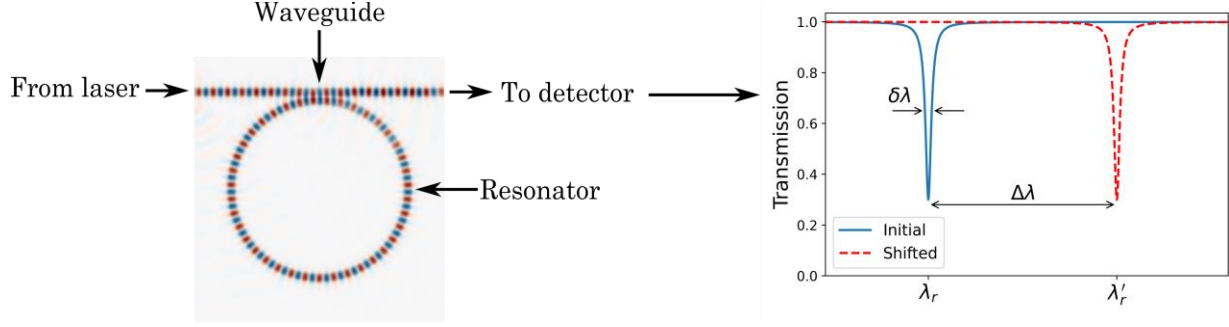


Figure 1.4: Snapshot of a simulation of a waveguide-coupled ring resonator undergoing WGM excitation and an idealized transmission spectrum showing a WGM dip and mode shift

is associated with the resolution of the resonator as a sensor. Narrower dips (higher Q) allow for the detection of smaller mode shifts and hence, higher sensor resolution.

#### 1.4. Previous WGM Sensors

Several sensors that rely on WGM shift have been proposed to measure a wide range of physical inputs, including pressure, [28] force, [24, 26] electric [23, 32] and magnetic field, [29, 30] acceleration, [31, 33] species concentration [25] and temperature [16, 27]. For pressure, two applications of WGMs have been demonstrated: a wall pressure and a static pressure sensor. In the former, a membrane that is exposed to a fluid flow compresses a micro-sphere on the other side, such that the pressure applied to the sphere by the membrane is proportional to the WGM shift due to deformation [40]. In the latter, the deformation of the sphere due to hydrostatic pressure (uniform) is measured using the micro-spherical WGM sensor [28].

A force sensor has also been demonstrated by placing a micro-sphere between two metal plates and compressing it in the poles such that the equatorial radius, where light is coupled, changes causing WGMs to shift [26]. An ultra-sensitive force sensor was also realized by testing resonators of different dielectric materials [24]. Extensive efforts have also been invested in electric field measurement using WGM shift [23, 32, 46]. The concept has been demonstrated by placing a micro-sphere between two electrodes, which creates an external electric field that deforms the sphere by electrostriction, defined as "elastic deformation

(strain) of a dielectric material under the force exerted by an electrostatic field” [46]. Magnetic field WGM sensors have also been proposed. Like the electric field sensors, a polymeric micro-sphere, containing a conducting shell [30] or embedded with polarizing particles, [29] is placed between a permanent magnet and a coil that generates a static or oscillating magnetic field. The conducting shell or polarizing particle causes the sphere to deform in the presence of a B-field, which translates to WGM shifts in the signal.

A WGM-based accelerometer has also been investigated by attaching a polymeric micro-sphere to a rigid base. The acceleration of the base causes the sphere to deform, so a relationship between acceleration and WGM shift is established [31]. In this approach, the sphere resonator acts as a transducer. In velocity measurement, a proof of concept sensor based on Doppler and WGM shift has been demonstrated by collecting light scattered from a moving object. A WGM resonator filters the scattered or reflected light from the target and the location of the dips changes due to the Doppler shift or object’s velocity [59].

In biology, WGM sensors have been used for nanoparticle detection, which has the potential to identify viruses [17]. A species concentration sensor based on WGM has been developed based on second-order effects. The efficacy of a WGM concentration sensor was tested by placing a micro-resonator in deionized water and incrementally adding potassium carbonate solution. The WGM shift, caused by changes in the refractive index of the surrounding medium, was then measured to determine the concentration of the added solution [25].

WGM sensors are useful for detecting physical changes of their environment. They are a sub-category of opto-mechanical transducers that can create a complete sensor when combined with optoelectronic systems. Since much theoretical and experimental work has been carried out to understand WGMs better, most applications focus on transmitting mechanical inputs to the fiber-coupled resonators. This dissertation considers the on chip integrated waveguide-coupled ring resonators as sensors. Configurations that rely on both physical deformation of the resonator chip and those where the chip is rigid are investigated.

## Chapter 2

### Photonic Seismometer

WGM resonators with ultra-high  $Q$  offer excellent measurement resolution. Their narrow linewidth allows for the detection of very small mode shifts related to minute changes in their morphology. Given their sensing potential, WGM resonators present an attractive solution for applications requiring high measurement resolution, such as seismology, when measuring weak seismic events (e.g., microseism).

In addition to their sensing capabilities, integrated micro-resonators offer the benefit of compactness and ruggedness thanks to the modern monolithic microfabrication processes. Ring resonators made of Si and Si-based materials can have diameters as small as 10's of  $\mu\text{m}$  and can be employed to realize highly compact sensing elements. Furthermore, micro-resonators are robust since they are made of glass materials and rely on mechanically stable waveguide-resonator, waveguide-fiber, and fiber-to-fiber optical couplings. Also, passive photonic resonators allow for low-power consumption sensing because they only require a minor percentage of light emitted by a typical telecommunication laser. Additionally, photonic circuits present the potential for easy integration of secondary sensors (e.g., temperature and pressure) that can improve the robustness of the primary sensor (e.g., optical seismometer). These potential benefits from WGM-based photonic sensors strongly suggest that they should be considered for applications such as seismic data acquisition in challenging conditions.

This chapter discusses the concept of an intrinsic all-optical cantilever based WGM seismometer and an analysis of the performance of a benchtop prototype. Static and dynamic characterizations of the seismometer are performed to assess the sensitivity and response. Finally, the results from the sensor calibration, supported by computational models, are presented. An additional experiment demonstrating the potential usage of an in-house micro-fabricated cantilever with improved performance is also included. All the results presented

here were obtained in laboratory conditions.

## 2.1. Seismometer Concept

The sensor proposed here operates based on the strain of a ring resonator embedded in a silicon substrate, as shown in Fig. 2.1. The chip with the ring resonator has a cantilever section and a proof mass attached to the tip. The chip carrier shown is attached to a base for which motion is monitored. For an Euler-Bernoulli cantilever beam, the axial strain is defined as [45]:

$$\epsilon_{xx} = -h \frac{d^2w(x)}{dx^2}, \quad (2.1)$$

where  $h$  is the distance from the neutral axis (zero stress plane) and  $w(x)$  is the transverse deflection related to the applied load ( $P$ ) at the free end by:

$$w(x) = \frac{P}{6EI} x^2 (3L - x), \quad (2.2)$$

and  $E$ ,  $I$ , and  $L$  are the Young's modulus, area moment of inertia, and length of the beam. For a load applied at the tip, the axial strain becomes

$$\epsilon_{xx} = -h \frac{P(L - x)}{EI}, \quad (2.3)$$

and can be related to the acceleration of a proof mass attached at the free end, which generates the load  $P$ .

The ring resonator acts as a strain gauge that monitors the deformation of the optical chip due to an applied load (see Fig. 2.1). Equations (2.1) and (2.3) show that the local strain is linearly proportional to the load (for small deflections) which, in our sensor, is generated by the acceleration of the proof-mass relative to the base. For a cantilever beam with a proof-mass, the equation of motion is expressed in terms of the tip/mass displacement,

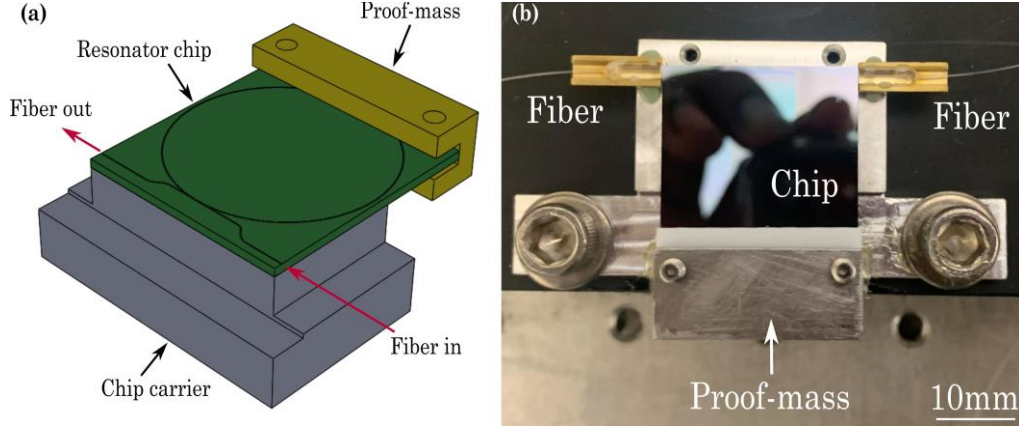


Figure 2.1: 3D rendering of the sensing element (a) and top view photograph of the assembled seismometer (b).

$y_m = w(L)$ , relative to the motion of the base [10]:

$$y_m'' + \omega_n Q_m^{-1} \dot{y}_m + \omega_n^2 y_m = -\ddot{y}_b, \quad (2.4)$$

where  $\omega_n$ ,  $Q_m$ , and  $\ddot{y}_b$  are the undamped natural frequency of the first vibrational mode of the beam, the mechanical quality factor of the system, and the acceleration of the base, respectively. The response of the system under consideration is used to identify the system parameters  $Q_m$  and  $\omega_n$ . It can be shown that the strain term in equation (1.2) is linearly proportional to the tip displacement. Thus,

$$y_m = A \frac{\Delta\lambda}{\lambda}, \quad (2.5)$$

where  $A$  is a constant. The motion of the base (acceleration) is assessed directly from the mode shift.

Equation (2.4) indicates that parameters  $Q_m$  and  $\omega_n$  characterize the sensor's response to the base motion. The vibration of mechanical structures always involves damping related to multiple loss factors that affect  $Q_m$ . For silicon plates, such as our optical chip, the effective damping is

$$\frac{1}{Q_m} = \frac{1}{Q_{TE}} + \frac{1}{Q_{air}} + \frac{1}{Q_{clamp}} + \frac{1}{Q_{other}}. \quad (2.6)$$



The terms on the right side of Eq. (2.6) are defined as losses due to: the thermoelastic effect resulting in temperature gradient (heat transfer) between sections of the beam under tension and compression, air-beam interaction, transfer of energy from beam to clamp, and other factors such as internal material friction. It is important to establish that equation (2.4) serves primarily as a mathematical model that is useful to compare various mechanical systems. In particular, the viscous damping (i.e., force proportional to velocity) term is a convenient and intuitive way of estimating the ability of the system to suppress the increased response near and at resonance. Expressions for the relevant damping mechanisms are provided in the literature.

An analytical solution for the thermoelastic damping of thin beams is given by [34] as

$$Q_{TE} = \frac{\rho C_p}{\alpha_T^2 T_0 E} \frac{6}{\xi^2} - \frac{6 \sinh \xi + \sin \xi}{\xi^3 \cosh \xi + \cos \xi}^{-1} \quad (2.7)$$

and,

$$\xi = H \sqrt{\frac{\omega_n \rho C_p}{2 \kappa_{th}}}. \quad (2.8)$$

The terms  $\rho$ ,  $C_p$ ,  $\kappa_{th}$ , and  $\alpha_T$  are the density, specific heat, thermal conductivity, and thermal expansion coefficient, respectively.  $Q_{TE}$  can be calculated using the material properties presented in [12].

The air dissipation is determined from the analysis provided by [54] based on [18] derivation for the viscous regime. For these conditions, the viscous damping is estimated by

$$Q_{air} = \frac{\rho H W^2 \omega_n^2}{3 \pi \mu W + \frac{3 \pi W^2}{4} \frac{2 \rho \mu \omega_n}{a}}, \quad (2.9)$$

where  $\mu$  and  $\rho_a$  are the dynamic viscosity and density of air, respectively.

The support loss depends on the cubic power of the length-to-height ratio of the beam and is expressed as [42]

$$Q_{clamp} = \kappa \left( \frac{L}{H} \right)^3, \quad (2.10)$$

where  $\kappa$  is an empirical parameter related to the geometry of the beam. For a rectangular geometry like the one discussed here, the values of  $\kappa$  lie in the range of 0.34-2.17.

Other contributions are neglected because of their high  $Q$  values (typically  $10^5$ - $10^9$ ). The reported value of the structural damping of silicon ( $\eta = 1/Q_{bulk}$ ) is  $5 \times 10^{-6}$  and can therefore be ignored [7]. However, the optical chip is attached to the carrier (see fig. 2.5a) by a layer of epoxy ( $\eta = 0.0368$  [39]) that could potentially introduce additional losses usually absent in micromachined monolithic cantilevers. The discussed loss factors will be compared to the measured  $Q_m$ , determined from the width of the resonance peak or the decay rate of the displacement amplitude of the beam under impulse excitation.

## 2.2. Sensor System

The sensing element consists of a cantilevered optical chip with an embedded waveguide and ring resonator. A section of the bottom face of the chip is attached to an aluminum carrier, resulting in an overhang (or cantilever) to which the proof-mass is attached. The chip is fiber-pigtailed to facilitate the coupling of light into and out of the waveguide as well as to provide a robust optical signal.

The chip is composed of a silicon (Si) substrate with a thin silica ( $\text{SiO}_2$ ) layer at the top, inside of which the silicon nitride ( $\text{Si}_3\text{N}_4$ ) waveguide and ring resonator are located. The dimensions of the chip are  $27 \text{ mm} \times 25 \text{ mm} \times 1 \text{ mm}$  ( $L \times W \times H$ ), with an 11 mm long overhang. The radius of the resonator is 12 mm.

Figure 2.2 illustrates the optoelectronic configuration of the prototype seismometer. A waveform generator modulates (typically 1 kHz ramp or sine) the wavelength of the light emitted by a continuous wave 1310 nm distributed feedback (DFB) diode laser. A 90:10 beam splitter divides the laser into two, and the 90% channel feeds the chip to excite the WGMs of the ring resonator. The output light from the chip goes to photodetector PD2. Similarly, the 10% light is directly coupled to PD1 and is a reference to remove the modulation profile from the WGM signal. A 12-bit analog-to-digital (A/D) converter acquires all the signals. The modulation signal triggers and synchronizes the acquisition of the photodiode signals. A

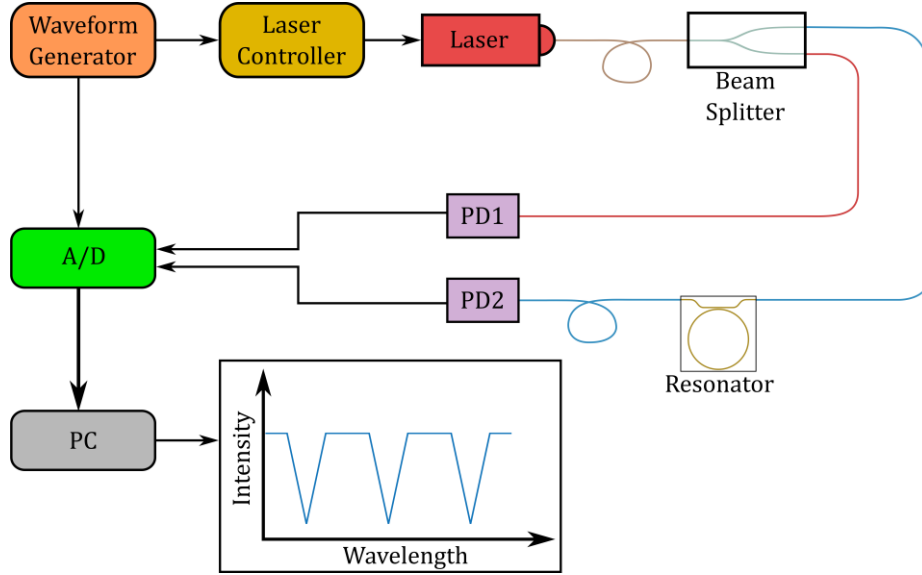


Figure 2.2: Schematic of the sensor system.

personal computer (PC) connected to the A/D records the data for post-processing analysis.

### 2.2.1. Signal Processing

Although real-time signal processing has been demonstrated for high-speed transient WGM sensing [2], a post-processing approach is chosen in this study to perform various data analyses and develop, compare, and optimize different signal processing techniques.

Three approaches were considered: dip detection (DD), cross-correlation (CC), and Lorentzian fit (LF). While DD is the fastest algorithm among the three, it is also the most susceptible to noise since it consists only of tracking the location of the minimum of the resonance dip (Fig. 2.3). The location of the minimum can exhibit fluctuations due to noise in the amplitude of the signal.

In CC, the mode profiles in the top of graph Fig. 2.3 are inverted into cross-correlated peaks to obtain the curve in the middle plot. The location of the maximum determines the relative shift between the reference and the shifted WGMs. The CC algorithm performs well, with lower noise than DD, but requires longer computation times.

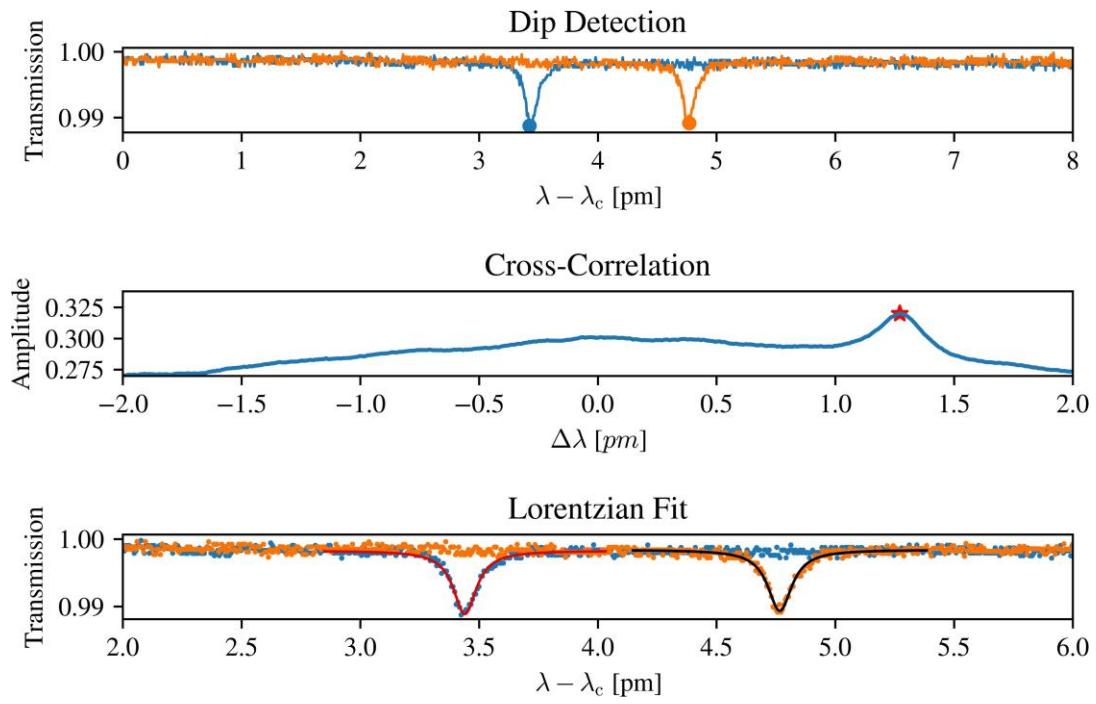


Figure 2.3: Demonstration of (top) DD, (center) CC, and (bottom) LF signal processing algorithms for automatic WGM shift measurement.

Finally, the LF algorithm is the most robust since it considers the overall profile of the resonance (instead of just a single point). This algorithm relies on fitting a Lorentzian function to the WGM dip (or peak) to obtain the resonant wavelength. The main drawback of LF is that it requires significant computational time and resources because of its iterative nature. For real-time applications, both DD and CC are suitable, with CC being favored because it can easily be configured to measurements exceeding the free-spectral-range of the WGMs [2]. Additionally, hardware realizations of CC circuits are now available [3], which could help reduce the computational demand of the envisioned seismograph.

## 2.3. Results

The sensing element is characterized using various approaches. A static analysis is employed to assess the force sensitivity of the resonator, which can be compared to other WGM sensors and to estimate the mass required to generate meaningful WGM shifts. The sensor is then tested in a series of dynamic experiments: harmonic excitation on a shaker table and impulse excitation with and without a damping block. The dynamic experiments allow us to determine the sensor's sensitivity, resolution, and frequency response. Finally, a preliminary in-house fabricated substrate is tested to demonstrate the sensing potential of a cantilever-based seismometer with a softer substrate.

### 2.3.1. Static Characterization

The apparatus shown in figure 2.4 is used to deform the optical chip and measure the tip deflection. A linear spring is employed alongside a motorized nano-translation stage to generate force. The displacement of the translation stage (compression/elongation of the spring) determines the magnitude of the force. A plastic mount transfers the spring force onto the chip, and Teflon sheets (or rubber pads) protect the chip from the metallic screws.

Figure 2.5a shows the spectral shift of the WGM caused by an applied force. The reference wavelength ( $\lambda_c$ ) is the initial location of the WGM dip. The resonance shift depends on the

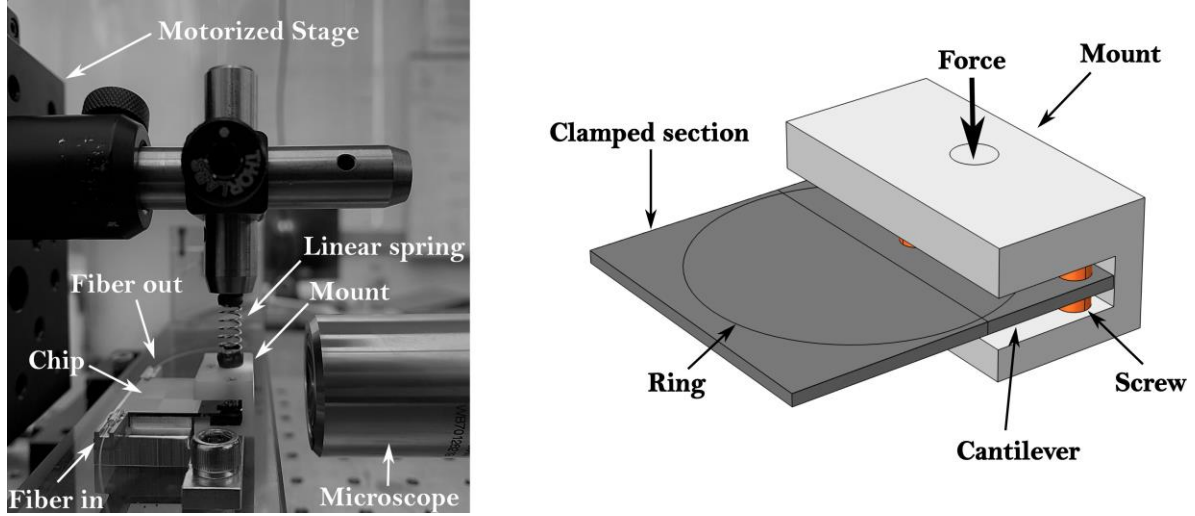


Figure 2.4: Apparatus employed for the determination of static force sensitivity (left) and geometry of 3D computational model (right).

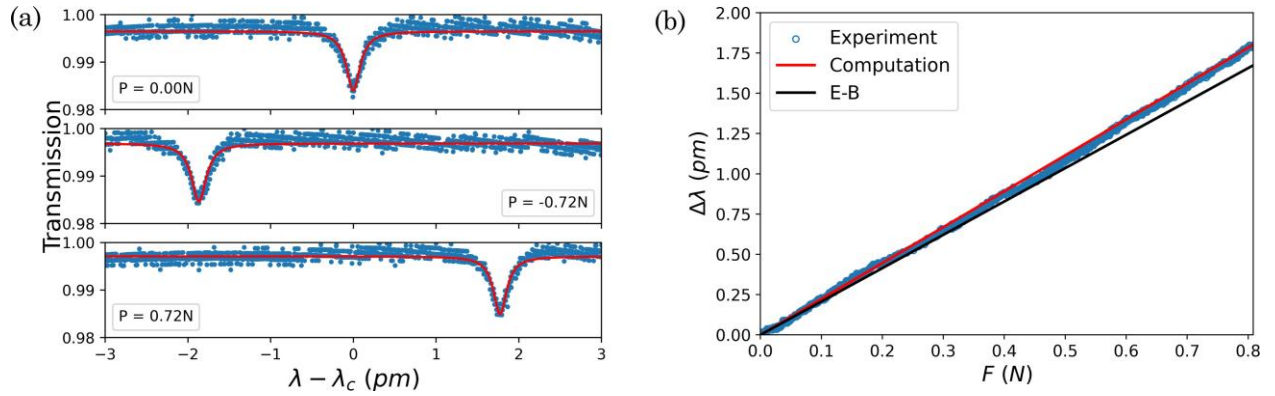


Figure 2.5: Shift of optical resonance due to force applied by linear spring (a), and measured WGM shift as function of the applied force (b).

magnitude of the force. A Lorentzian fit algorithm tracks the location of the resonances and determines the optical quality factor,  $Q$  ( $\sim 1.5 \times 10^7$ ).

Figure 2.5b shows the effect of the applied force on the WGM shift. Computational estimates of the mode shifts are also shown in the figure as a red line. Since equations (2.1) to (2.3) apply to 1D beams, for a more accurate model, the computations are performed by a 3D finite-element analysis (FEA) of the same geometry used in the experiments. The WGM shift is determined by computing the change in the circumference of a circle on the plate's top surface. The perimeter of the closed line before ( $L_i$ ) and after ( $L_f$ ) the deformation is calculated by integrating around the line ( $\oint dl$ ). The change in the perimeter is related to the WGM shift by

$$\Delta\lambda = \lambda \frac{L_f - L_i}{L_i}. \quad (2.11)$$

The fraction  $(L_f - L_i)/L_i$  represents the effective strain on the resonator. The estimated force sensitivity of the sensor is 2.23 pm/N. Due to the large thickness ( $\sim 1$  mm) of Si substrate, the force sensitivity is considerably lower than that of sphere WGM sensors demonstrated by [26]: solid silica (31 pm/N), solid PMMA (1087 pm/N) and hollow PMMA (7664 pm/N).

In addition to the finite element method (FEM) solid mechanics solver, the WGM mode shift is also estimated by a model based on Euler-Bernoulli beam equations. For this the cantilever geometry is simplified to a Si beam with a circle on the top surface representing the resonator. The origin lies in the symmetry plane that cuts the beam in half, parallel to the longitudinal direction, and intersects the neutral axis ( $h = 0$ ). The coordinates of the resonator before deformation can be determined using the equations of a circle. For a discrete set of points, the coordinates of the resonator are  $\mathbf{x}_r = [x_1, x_2, x_3, \dots, x_n]$ ,  $\mathbf{y}_r = [y_1, y_2, y_3, \dots, y_n]$ , and  $\mathbf{z}_r = [z_1, z_2, z_3, \dots, z_n]$ , such that the resonator before deformation is

$$L_i = \sum_{i=1}^n [(x_{i+1} - x_i)^2 + (y_{i+1} - y_i)^2 + (z_{i+1} - z_i)^2]^{1/2}. \quad (2.12)$$

After deformation, the new coordinates are obtained using the longitudinal and transverse components of the displacement,  $u(x) = -h \frac{dw(x)}{dx}$  [45] and  $w(x)$  (eq. (2.2)),

$$L_f = \sum_{i=1}^{N-1} [\{(x_{i+1} + u(x_{i+1})) - (x_i + u(x_i))\}^2 + \{y_{i+1} - y_i\}^2 + \{(z_{i+1} + w(x_{i+1})) - (z_i + w(x_i))\}^2]^{1/2} \quad (2.13)$$

Finally, the mode shift is estimated from equation (2.11), yielding a sensitivity of 2.08 pm/N. The agreement between the experimental data, the FEM solver, and the Euler-Bernoulli equations indicates that the simple model accurately predicts the behavior of the cantilever for small deformations.

### 2.3.2. Harmonic Excitation

A vibration table was used for the acceleration calibration of the seismometer in accordance with [56]. Figure 2.6 illustrates the configuration for this experiment. The prototype seismometer and a commercial MEMS accelerometer are attached to a base, which is rigidly connected to the vibration table. A harmonic signal from a waveform generator controls the motion of the table. The commercial accelerometer serves as a reference scale for calibration. In this preliminary experiment, a 25 g proof mass is used on the sensor, and no damping is employed.

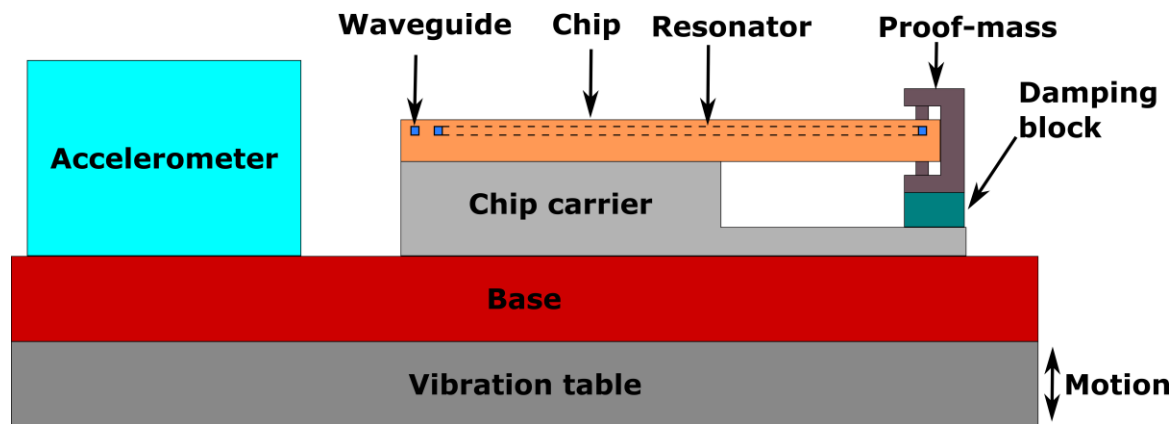


Figure 2.6: Schematic of the shake table experiment used for harmonic base excitation.



The laser is scanned at a rate of 1 kHz and the transmission spectrum is acquired at 5000 samples per cycle of the laser (or 5 MSamples/s), sufficient to resolve the WGMs. Each scan of the laser yields a single point in the WGM shift time evolution, so it is essential to ensure that the vibration table's motion is adequately resolved. In this calibration run, a 15 Hz harmonic signal from a waveform generator controlled the movement of the table. This results in 67 WGM data points per cycle of the table oscillation.

Figure 2.7a shows the time variation of the WGM shift and the corresponding accelerometer output. The result shows the efficacy of monitoring acceleration by tracking WGM shifts. The harmonic motion of the base results in a sinusoidal shift of the WGM. The phase difference between the two signals is attributed to the difference in mechanical impedances of the two systems. A cross-correlation-based algorithm is used to align the two signals (removing the phase between them), and the mode shift is plotted against the measured acceleration of the vibration table in Figure 2.7b. The linear fit yields a sensitivity of  $1.97 \text{ pm}/(\text{m}/\text{s}^2)$ , with a 2% rms error (or  $0.062 \text{ m}/\text{s}^2$ ). The relatively low sensitivity of the seismometer is due to the large stiffness of the 1-mm-thick substrate used in the present preliminary setup. The sensitivity may be increased by adjusting various parameters in the sensor design, including increasing the proof mass size, using a more compliant substrate, and adjusting the substrate material, thickness, and overhang length.

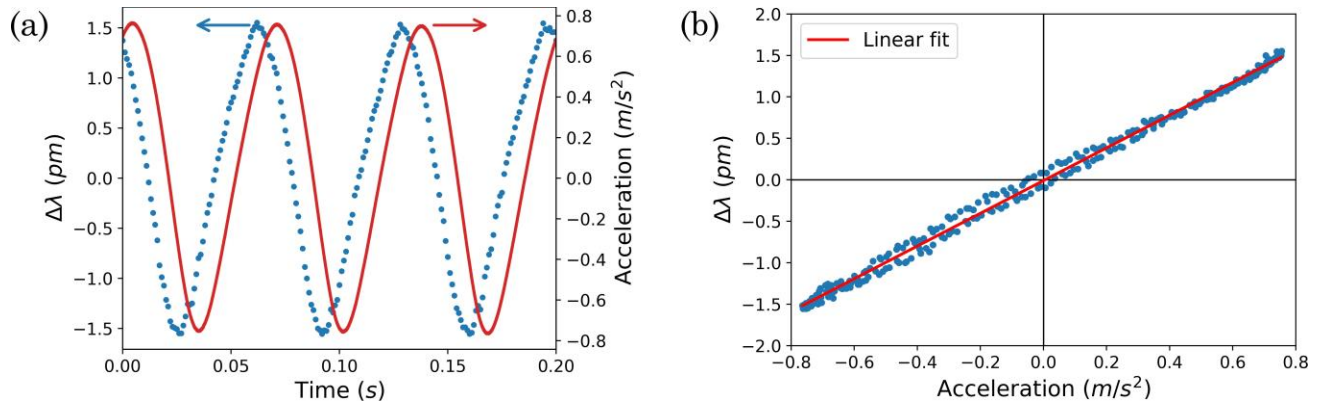


Figure 2.7: (a) WGM shift (circles) and acceleration of table (solid line); (b) Phase corrected plot of WGM vs measured acceleration. The solid line is the line fit. The small deviation of the experimental data from the line is attributed to the asymmetry in the clamping mechanism.

### 2.3.3. Free Vibration

The system parameters in equation (2.4) for the prototype sensor were determined using an impulse response experiment. An impulse force was applied to the proof mass, disturbing it from its rest position. The response of the sensor is observed by monitoring the WGM shift. Figure 2.8a shows the optical mode shift due to the perturbation of the proof mass. The impulse perturbation is applied around time  $t = 0.4$  s. The free vibration of the system given in equation (2.4) is [22]:

$$y_m(t) = y_o e^{-\omega_n Q_m^{-1} t/2} \sin(\omega_d t + \theta_o) \quad (2.14)$$

where  $\omega_d = \omega_n \sqrt{1 - (2Q_m)^{-2}}$  is the damped frequency. The constants  $y_o$  and  $\theta_o$  depend on the initial displacement and velocity. These parameters are calculated from the experimental data and used as input to a least-square-fit algorithm applied to equation (2.14). The WGM shift fitting yields the middle plot in figure 8b and the estimated  $Q_m$  and  $\omega_n$  are 26.6 and 135.87 Hz, respectively. For comparison, the value of  $Q_m$  from Equation (2.6) is  $\sim 26.68$ . The harmonic oscillator model agrees well with the experimental observations.

A frequency-domain analysis of the signal presented in figure 2.8b is also carried out. The frequency response of a harmonic oscillator due to an impulse input is [22]

$$|Y_m(\omega)| = \frac{B}{[(\omega^2 - \omega_n^2)^2 + (Q_m^{-1} \omega \omega_n)^2]^{1/2}}, \quad (2.15)$$

where  $B$  is a constant that accounts for the magnitude of the perturbation and has units of acceleration. Figure 2.8c shows the amplitude as a function of the frequency, suggesting that the amplitude is flat below 40 Hz. The amplitude increases significantly at resonance, which is not a desirable trait for seismometers, even though the seismic input can be calculated from the sensor's transfer function. Therefore, damping techniques suitable for the current configuration should be considered for future versions of the seismometer. However, the present preliminary results show the viability of the cantilever substrate, with an embedded ring resonator, as a miniature photonic seismometer.

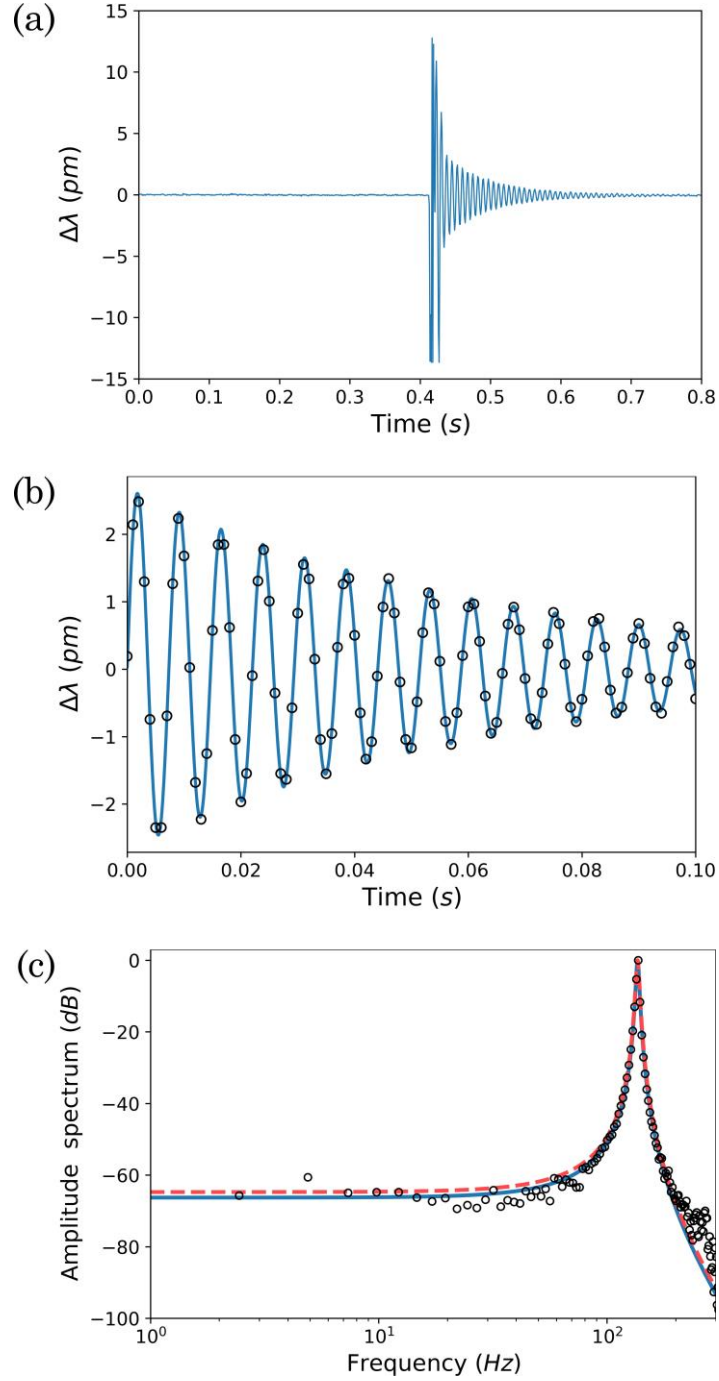


Figure 2.8: (a) Free vibration of the seismometer; (b) Ring down fitting of equation (2.14) (solid line) and experimental values (circles); (c) Peak normalized frequency response from experiment (circles), equation (2.15) with estimated parameters from (2.14) (solid line), and analytical  $Q_m$  (dashed line). The response of the prototype photonic seismometer agrees with the spring-mass-damper model and is linear up to approximately 40 Hz.

#### 2.3.4. Resolution and Dynamic Range

The sensor resolution can be estimated from the WGM shift noise floor and sensitivity. For the current prototype, the WGM shift rms noise, in the absence of a proof mass and any mechanical excitation, is 4.94 fm for a laser scanning rate of 200 Hz, which corresponds to 2.5 mm/s<sup>2</sup> based on the sensitivity of 1.97 pm/m/s<sup>2</sup> (Fig. 2.7b). This scanning rate is selected to be comparable to the bandwidths of the SEIS-SP and mainstream geophones such as the SM-24.

The spectral analysis of the noise did not show a strong frequency dependence and had a spectral density of  $\sim 80 (\mu\text{m/s}^2)/\text{Hz}^{1/2}$  (or  $8.2 \mu\text{g}/\text{Hz}^{1/2}$ ). This preliminary noise assessment likely overestimates the measurement resolution since there is noise contribution from multiple sources: flow of air around the sensing element, thermal fluctuations of ambient conditions, vibration of devices in the laboratory, oscillation of the building, and urban activity. Some of the noise sources will be addressed once the sensor is enclosed. At the same time, the effect of fluctuations in ambient conditions can be compensated for by a reference resonator [50]. The seismic noise level should be significantly lower in observatories where we intend to test the sensor.

The elastic range of the beam limits the dynamic range of the sensor. In the current configuration, the seismometer does not have mechanical stops to prevent the excessive deformation of the beam but once added, the goal would be to constrain the motion to avoid non-linear deformation. [43] reports an average bending strength of 470 MPa for mm-scale Si cantilevers. Based on this information, a reasonable limit for the present cantilever is 235 MPa (50% safety factor), corresponding to a maximum shift of 143 pm based on a numerical beam model accounting for geometric nonlinearities (i.e., large deformation). Since the rms noise is the measurement resolution, the estimated dynamic range is 90 dB. Improvements on the dynamic range can be achieved by reducing the sensor noise floor (e.g., using a resonator with larger Q) and increasing the sensitivity by selecting different substrate materials and optimizing the proof mass.

### 2.3.5. Damping

The results presented above for the current silicon cantilever prototype show that the sensor has very low intrinsic damping. Therefore, additional damping needs to be integrated into the system for an improved performance. In the present study, as an initial attempt, a 1 mm-thick polydimethylsiloxane (PDMS) slab is added between the proof mass and the chip carrier to flatten the resonance (see Fig. 2.6). The PDMS block has a 20:1 base-to-curing-agent mass ratio with a loss tangent of 0.2-0.5 [48]. Figure 2.9 shows the free vibration of the sensor with a 70 g proof-mass with and without the damping block. When the PDMS block is included,  $Q_m$  decreases from 17.5 to 11.5, while  $\omega_n$  shifts from 79 to 90 Hz.

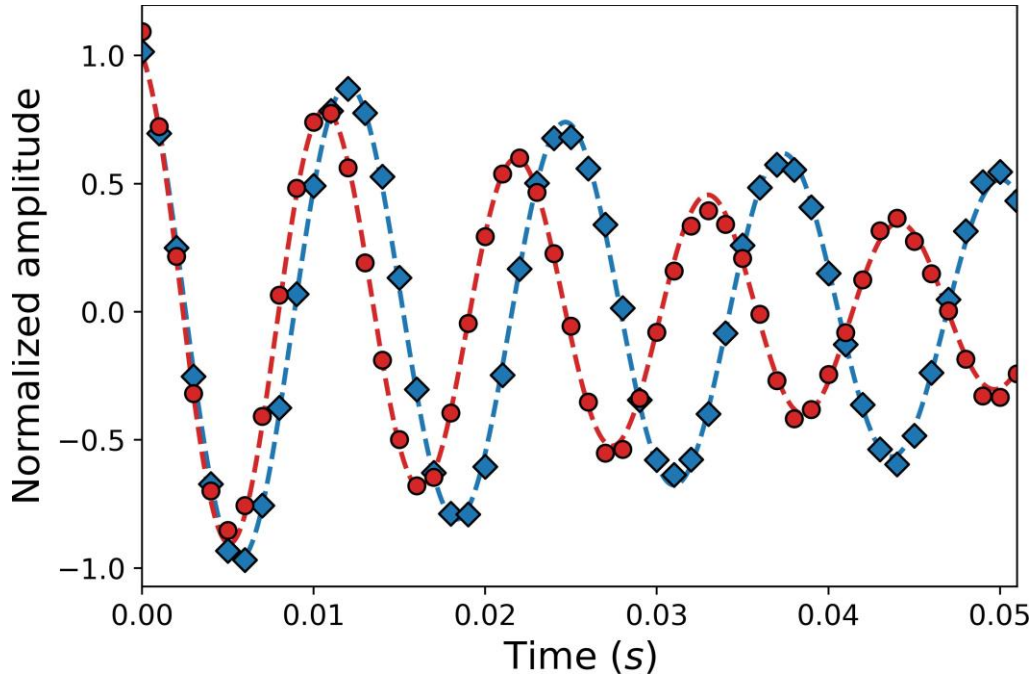


Figure 2.9: Normalized amplitude of sensor response before (blue) and after damping (red). The solid lines are fit of Eq. (2.14). The inclusion of a PDMS block between the proof-mass and the chip carrier introduces additional damping into the sensor.

While the damping structure improves the system's response, it does so at the expense of sensitivity. This can be attributed primarily to the relation between the loss tangent and the complex Young's modulus (storage and loss) of the material, which factors into the  $\omega_n^2 \gamma$  term of eq. (2.4). Reference [53] provides a model where the structural damping

( $\eta = 1/Q_{bulk}$ ) is represented by a complex spring stiffness and shows that increasing  $\eta$  leads to slightly higher (less than 1%) damped natural frequencies. However, in our experiment, the observed significant shift in natural frequency ( $\sim 13\%$ ) is primarily due to the introduction of the damping block leading to higher effective stiffness. Although this effect could be mitigated by increasing the mass to prevent loss of sensitivity, different damping approaches should also be investigated for an enhanced sensor design.

Alternatives to hysteretic damping could flatten the mechanical resonance (2.8c) without significantly affecting the sensitivity. The squeeze film effect - dissipation of energy due to motion of fluid between a fixed and a vibrating surface - [4] presents an attractive solution for the present sensor since it does not require adding new components but rather an improved geometric design. Alternatively, placing the sensing element in a container filled with liquid or pressurized gas could improve the viscous damping [54]. Still, practical considerations are necessary to ensure no leakage from the sensor enclosure. These damping mechanisms would significantly improve the performance of our sensing element while allowing it to remain passive.

#### 2.3.6. Computations on a Raspberry Pi 4

The proposed sensor's primary target application is remote sensing with limited computational resources. Therefore, assessing the computational requirements for effective sensor performance is necessary. For this purpose, a Raspberry Pi 4 is employed to compute the WGM shifts of the signals previously recorded by the analog-to-digital converter (A/D) in Fig. 2.3. The signal processing algorithms discussed earlier are tested. The results show good agreement between all three approaches, with an average computational time close to the sampling period of the WGMs ( $\sim 1$  ms). This suggests that the WGM shift can be determined in pseudo-real-time, either by a dedicated digital/analog circuit or a mini-computer such as the Raspberry Pi.

#### 2.3.7. Thin SiO<sub>2</sub>-Si-SiO<sub>2</sub> Beam

In the present demonstration, the 19  $\mu\text{m}$ -thick  $\text{SiO}_2$  optical layer (with the bus waveguide and the ring resonator) is grown over a commercially available 1 mm-thick Si substrate. For a given proof mass, using thinner Si substrates improves the sensitivity of the cantilever system. As a demonstration of the sensitivity potential of the current sensor approach, a preliminary plate is fabricated in-house to have a lower stiffness. The plate consists of a 110  $\mu\text{m}$ -thick Si substrate with an 8  $\mu\text{m}$   $\text{SiO}_2$  layer grown on each side, one of which would house the waveguide and resonator. Figure 2.10a is a scanning electron microscope photograph of the cross-section of a representative sample plate.

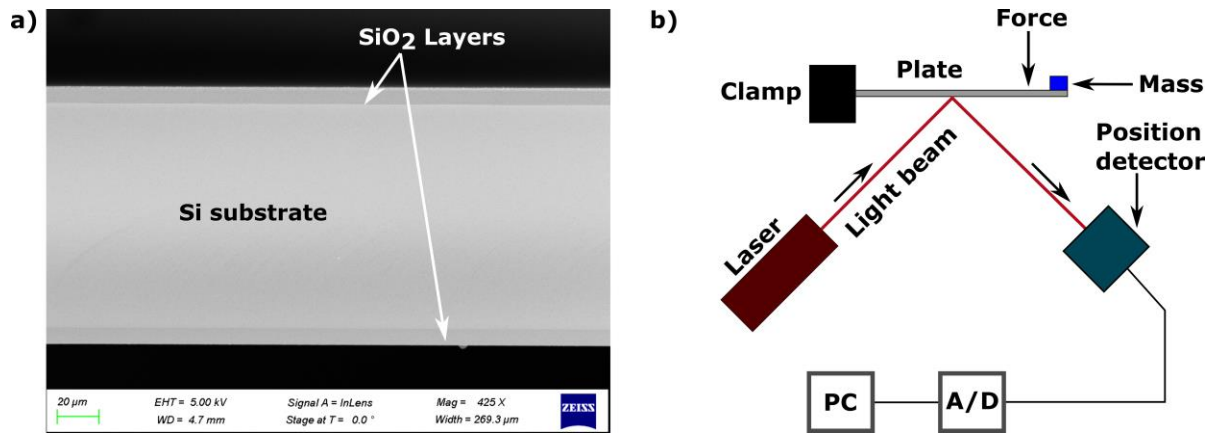


Figure 2.10: (a) Cross-section of a representative thin beam sample; (b) Schematic of apparatus used to measure the response of the thin plate.

Fig. 2.10b illustrates the configuration used for the dynamic characterization of the plate. Light from a 640 nm continuous-wave laser is reflected from the surface of the sample to an optical position detector. The free vibration of the system is measured by disturbing the plate and recording the signal from the detector. The plate dimensions are 3 cm  $\times$  1 cm  $\times$  126  $\mu\text{m}$  with a 2.5 cm-long overhang. A 230 mg proof-mass is added at the free end of the beam. Fig. 2.11 is a plot of the peak normalized frequency response alongside a fit of eq. (2.15) with  $Q_m = 88$  and  $\omega_n = 59.4$  Hz.

A computational model was used to estimate the performance of the thin plate seismometer. The approach employed is the same as the one in the previous experiments. A circular line on the plate's top surface represents the ring resonator as previously described. For



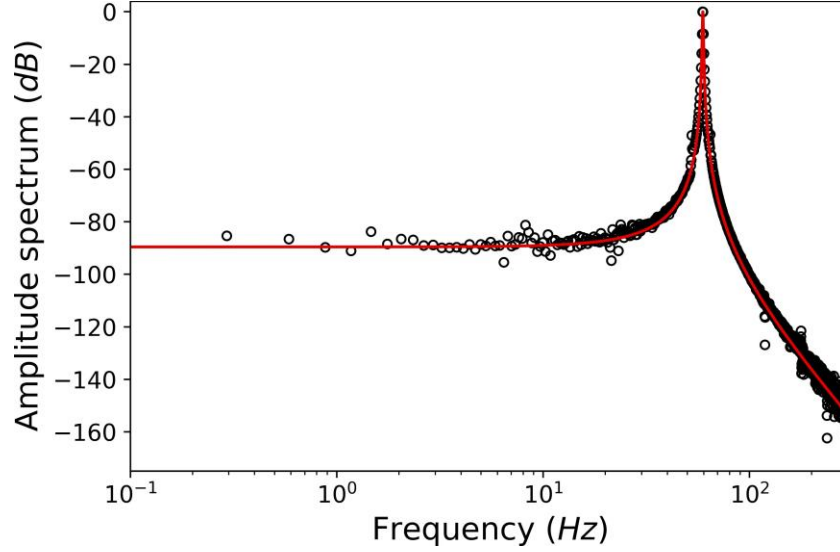


Figure 2.11: Amplitude spectrum of thin cantilever vibration under impulse excitation. The solid line is the fit of Eq. (2.15). For the thin plate  $\omega_n = 60$  Hz with a proof-mass of 0.25 g. For comparison, the thick beam required a 70-g proof-mass to reach  $\omega_n = 80$  Hz.

the static case, force is applied on the free end, while for the dynamic one, an acceleration is prescribed to the clamped section of the plate. The calculated force and acceleration sensitivities are 5.5 nm/N and 2.42 pm/m/s<sup>2</sup>, respectively. Owing to its lower stiffness, the thin-plate sample performance is superior to that of the 1 mm-thick plate. Thus, soft substrates should be employed to develop highly sensitive sensing elements that allow us to target small-magnitude seismic events in different frequency bands potentially.

#### 2.3.8. Nonlinearity Considerations

The analysis presented with equations (2.1) to (2.5) is the solution to small deformations where a linear analysis is used. Typically, the proof mass displacement is physically limited by mechanical stops in seismic instruments to avoid nonlinearities. The same approach would be used for the proposed sensor when building a field-ready device. Allowing large deformations would make a practical and easy-to-use implementation of the current sensor concept difficult. In addition to the increased complexity in signal processing, nonlinearity could also lead to damage to the sensor, especially when considering the amplification of motion for the low-damping cantilever discussed here.



When non-linear deformation is desirable or allowed, [61] a modified version of equation (2.4) is required. The large deformation can be accounted for by including two terms  $c_1 y_m$  and  $c_2 y_m^2$  that depend on the displacement. This model helps remove the effect of non-linear deformation (up to a quadratic power) and reliably estimates the sensor response. Nevertheless, it is not desirable to have arbitrarily large deformation, and seismometers are designed to operate in the linear range.

## Chapter 3

### Evanescent Field-Based Sensing

WGM resonators exhibit an evanescent tail in which a portion of the optical modes travel outside the cavity adjacent to the interface between the resonator and the surrounding medium. Depending on the resonator geometry, the evanescent field can be interacted with using a dielectric material. This chapter presents a sensing approach that relies on evanescent field perturbation where a dielectric object (perturber) extends into the evanescent tail of the microresonator. In this approach, unlike the one discussed in the previous chapter, the position of the perturber rather than the morphology of the resonator is modified (by a change in the measured property), inducing a shift in the WGM. This approach is suitable for applications in which the deformation of the resonator is neither feasible nor desirable and can be used for both three-dimensional (e.g. spheres, toroids) and planar (e.g. disks, rings) resonator geometries.

This chapter investigates, through analysis and experiments, the feasibility of this sensor approach for both geometries by using a sphere resonator (directly exposed to air) and an on-chip ring-resonator. In the experiments the modes of the resonators are perturbed by a dielectric spherical perturber, such that the motion of the perturber across the evanescent tail on the resonators' outer surface leads to a measurable shift in the resonators' WGM. In the ring experiment, a ferromagnetic structure is attached to the perturber stem so that the system enables the detection of magnetic field variations.

#### **3.1. Sensor Concept**

The sensor's optoelectronic configuration is the same as that described by Fig. 2.2. Further, the ring resonator is the same as that used for the seismometer described in Chapter 2. However, the change in the effective index ( $\Delta n/n$ ), rather than the mechanical strain

( $\Delta R/R$ ), causes the WGMs to shift (see Eq. (1.2)). The presence of a dielectric object in the evanescent field, in effect, perturbs the effective refractive index. Similarly, a dielectric sphere is also employed to demonstrate a controlled evanescent field perturbation, providing a comparison for two different resonator geometries: planar and three-dimensional.

In the typical chemical or biological photonic sensors, the measurement is accomplished by monitoring the WGM shift induced by a change in the dielectric property of the medium surrounding the resonator [25,41] or by the attachment of a particle on the outer surface of the resonator [55]. In the latter, the particle is typically static inside the evanescent field and its placement is not carefully controlled. However, for the measurement of mechanical quantities (e.g., force or acceleration), a careful and controlled perturbation of the evanescent field is required. The sensor concept proposed here addresses the challenging aspect of controlled perturbation and presents a configuration suitable for measuring mechanical parameters such as displacement and force.

### 3.2. Numerical Analysis

A 2D axisymmetric model was solved using a finite element method (FEM) software for the geometry shown in Fig. 3.1. The left, center, and right figures show the perspective, top, and side (cutaway) views, respectively. Computations were carried out for both sphere and ring resonator configurations, as shown in the figure.

The 2D ring resonator is the same one used in Chapter 2. The  $\text{Si}_3\text{N}_4$  ring is embedded in a  $\text{SiO}_2$  layer and located  $2\text{ }\mu\text{m}$  below the top surface of the optical chip. Although very small, a portion of the evanescent field still extends past the top surface of the chip (extending into air). The 3D resonator is an  $861\text{ }\mu\text{m}$ -diameter  $\text{SiO}_2$  sphere ( $Q \sim 10^7$ ) coupled to a tapered fiber. The sphere is made by melting the tip of an SMF-28 optical fiber (both core and cladding) into a spherical shape. The rest of the fiber is used as the stem to hold the sphere.

For a given radial mode number, the WGM of an optical cavity surrounded by a medium with azimuthally varying refractive index can be expressed as [13]

$$\lambda_r = \frac{1}{2\pi} \int_0^{2\pi} \lambda_{res}(\phi) d\phi, \quad (3.1)$$

where,  $\phi$  is the azimuthal angle and  $\lambda_{res}$  is the WGM corresponding to the case when the surrounding medium has uniform refractive index equal to that for the angle  $\phi$ . The parameter  $\lambda_{res}$  is calculated for each incremental azimuthal angle taking into account the gap variation with  $\phi$  as depicted in figure 3.1 (right).

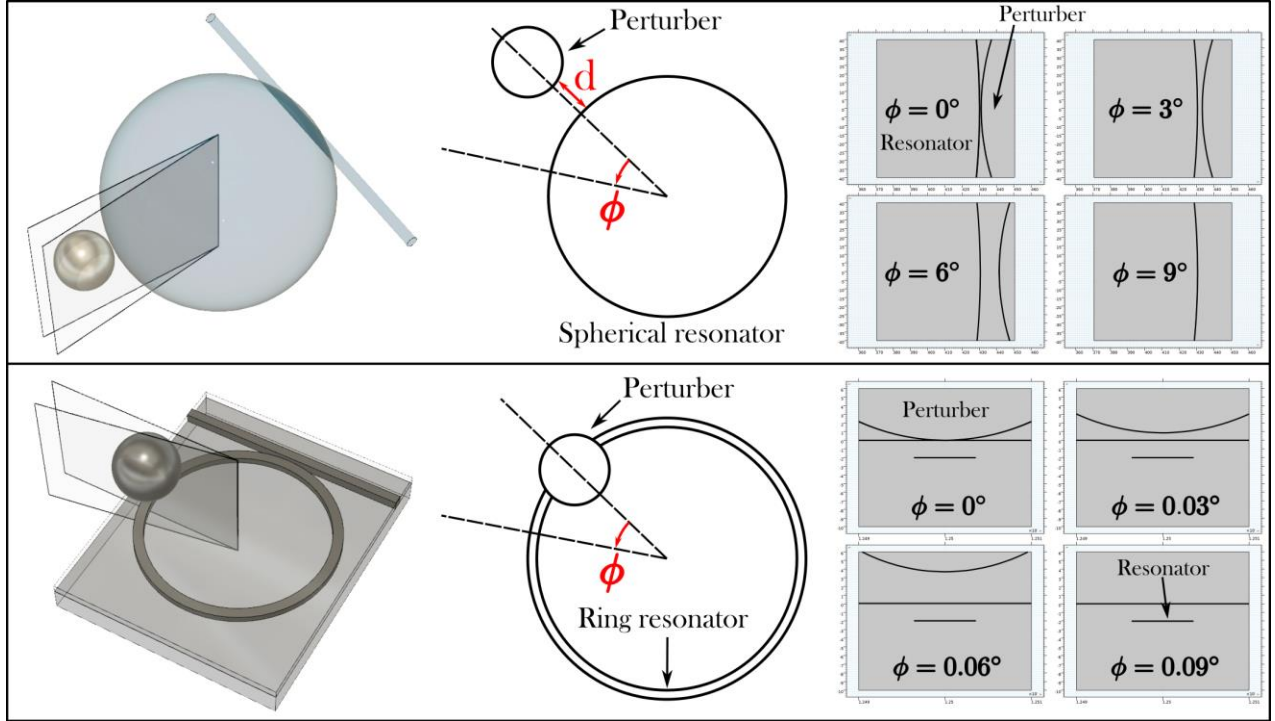


Figure 3.1: Geometry for the computational model for sphere resonator (top) and ring resonator (bottom). The left figures show a 3D rendering of the geometry under consideration. The center figures illustrate the top view of the geometry and the selection of azimuthal angles resulting in the right figures. The variation of the azimuthal angle leads to different cross-sections (varying gap between resonator and perturber).

When the gap is large enough to be outside of the evanescent field,  $\lambda_{res}(\phi) = \lambda_{res} =$  constant. The WGM shift,  $\Delta\lambda$ , for a given  $d$  is expressed as:

$$\Delta\lambda = \frac{1}{2\pi} \int_{\phi_0}^{\phi_0 + \Delta\phi_0} [\lambda_{res}(\phi) - \lambda_{res}] d\phi, \quad (3.2)$$

where the perturber interacts with the evanescent tail in the azimuthal angle range  $\phi_0$  and  $(\phi_0 + \Delta\phi_0)$ . The WGM values,  $\lambda_{res}(\phi)$ , are obtained across this  $\phi$  range (each representing a slightly different cross-sectional geometry) with an increment of  $0.05^\circ$ . By taking  $\phi_0 = 0$  as the line of symmetry in the computations, Equation (3.2) reduces to

$$\Delta\lambda = \frac{1}{\pi} \int_0^{\Delta\phi_0} [\lambda_{res}(\phi) - \lambda_{res}] d\phi, \quad (3.3)$$

where  $\Delta\phi_0$  is now half of the total interaction angle range.

### 3.3. Experimental Setup and Results

The extent to which the evanescent field extends past the bounds of the optical cavity depends on, among other parameters, the resonator's geometry. The evanescent tail is exposed to the medium surrounding spherical resonators and can be significantly interacted with using a dielectric object. Access to the evanescent tail for integrated resonators is reduced considerably or in some instances, may not even be possible since the resonator is typically protected from the outside environment by a top layer (usually  $\text{SiO}_2$ ).

Figure 3.2 compares the two resonator geometries employed throughout this part of the research. The top figures 3.2a and 3.2d show the geometries and refractive index profile of the sphere and ring resonators. The mode (electric) field distributions for both resonator geometries are shown in Fig. 3.2b and 3.2e. These profiles are obtained using an axisymmetric eigenfrequency electromagnetic wave solver that requires only the cross-section of the resonator. The field amplitude is normalized by the maximum value of the electric field norm in the mode. The evanescent tail for the sphere and ring resonator along the lines indicated in Fig. 3.2b and 3.2e are shown in 3.2c and 3.2f, respectively. As expected, the optical

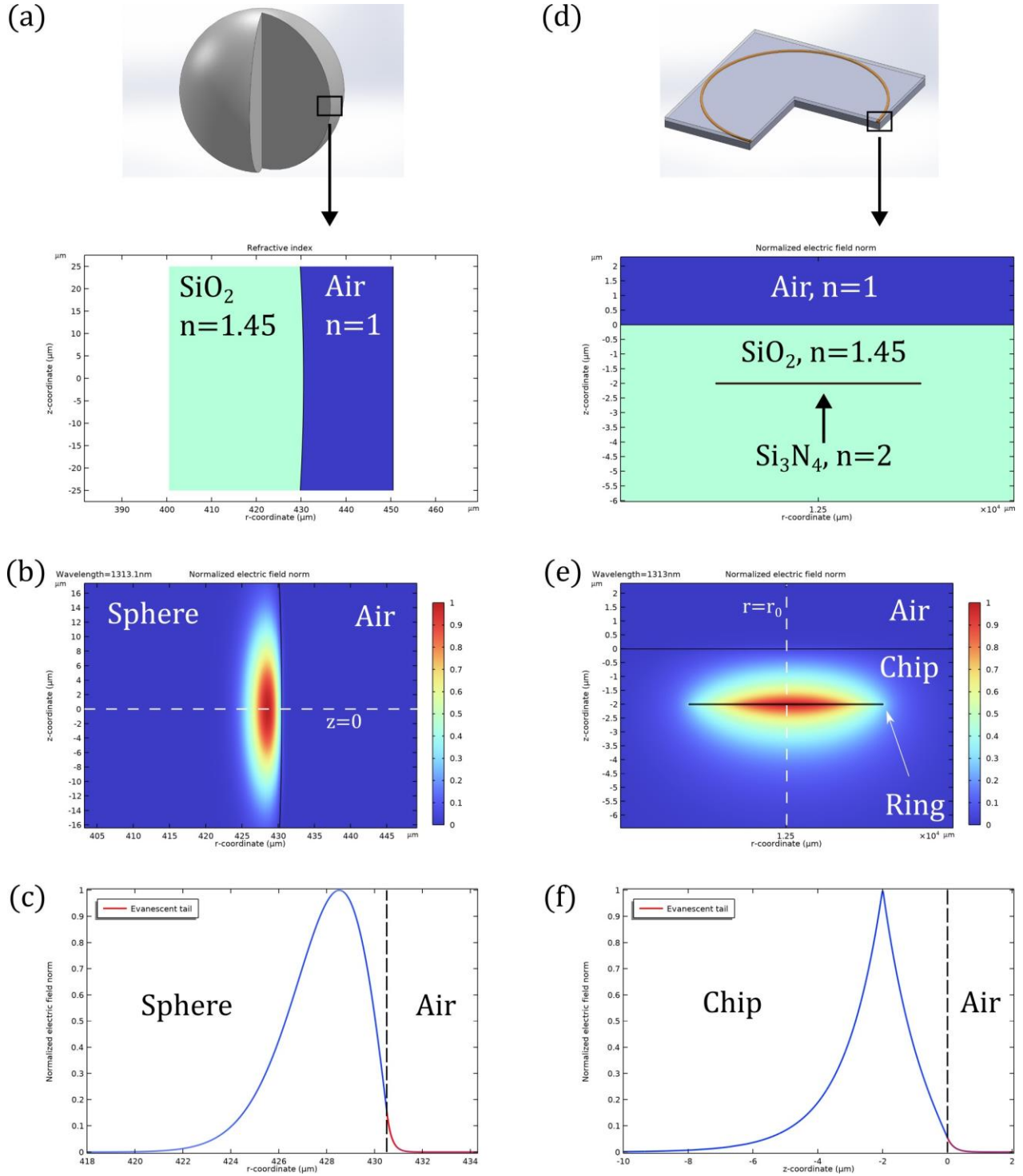


Figure 3.2: Computational analysis of the optical modes of a sphere (left) and an integrated ring (right) resonator. Resonator geometry and corresponding refractive indices (a,d); transverse electric field distribution (b,e); radial distribution of transverse electric field and evanescent tail (in red) (c,f).

mode of the sphere extends further into the surrounding medium than the ring resonator. Nevertheless, evanescent tail perturbation of both resonators is still possible by placing a dielectric object in their vicinity.

### 3.3.1. Sphere Resonator

The WGM resonator and the perturber are shown in 3.3a. The perturber is a 125  $\mu\text{m}$  diameter silica beam with a bulbous tip having an apex radius of about 137  $\mu\text{m}$ . The sphere resonator and the tip of the perturber are formed by melting the tip of an optical fiber (both the cladding and the core). As in the previous sphere resonator studies [23, 26, 29, 31], the laser light is evanescently coupled into the resonator using a tapered optical fiber, with  $\sim 8$   $\mu\text{m}$  diameter in the coupling region. The perturber is placed on a 3D translation stage with the in-plane motion controlled by motorized actuators. The perturber is moved towards the resonator and sweeps along the x direction are made at different resonator–perturber gaps.

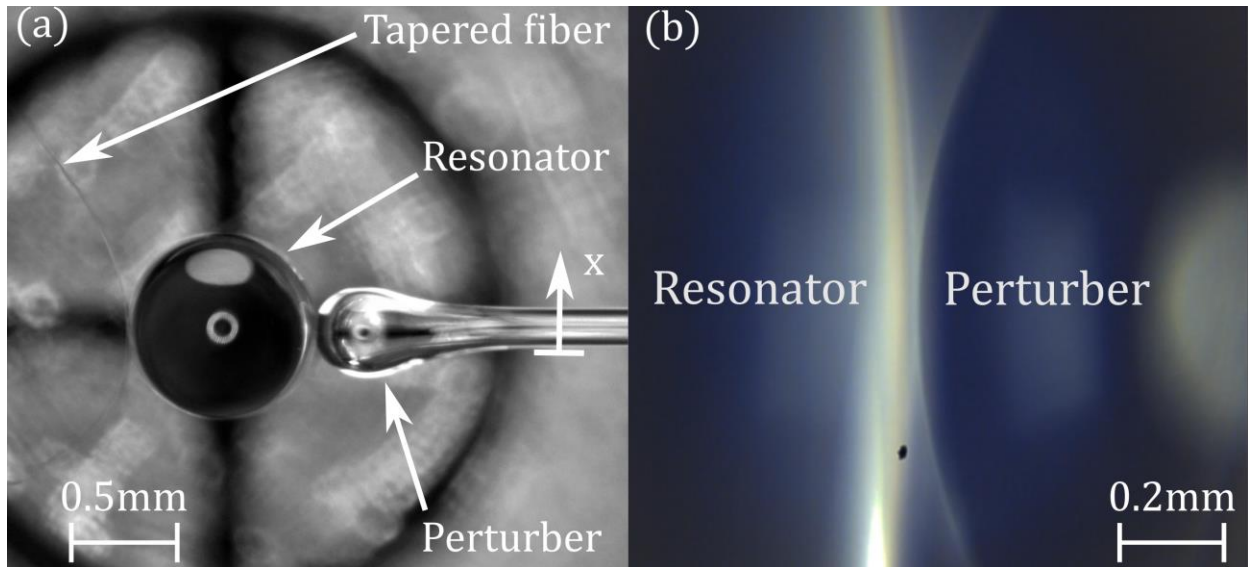


Figure 3.3: Photograph of sphere resonator and perturber: (a) top view of the sphere resonator coupled to tapered fiber on the left and a perturber on the right side; (b) side view and close up of sphere-perturber interaction region.

As the perturber moves along x-direction shown in Fig. 3.3a, its tip sweeps across the evanescent tail extending from the resonator's surface resulting in the WGM shifts observed



in Fig. 3.4. The inset shows two representative transmission spectra corresponding to the indicated positions on the graph. The configuration yields a maximum WGM shift of about 1.80 pm with good repeatability. If the smallest WGM shift that can be resolved corresponds to 1% of the resonance linewidth [19], this yields a measurement dynamic range exceeding 1000.

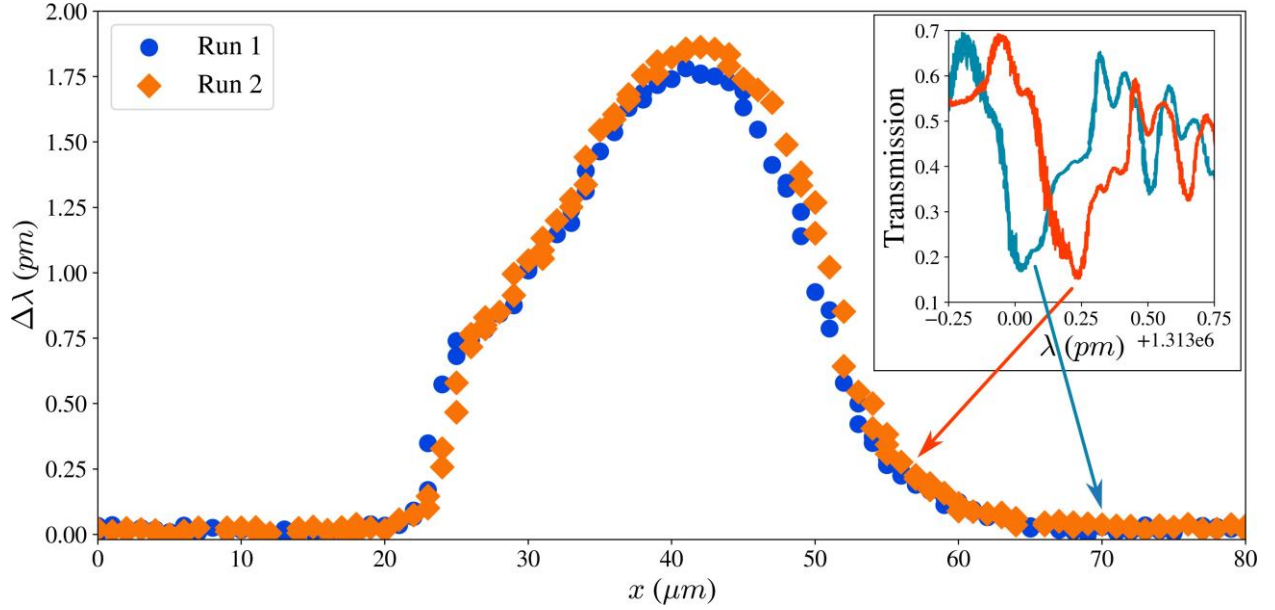


Figure 3.4: Experimental results for the perturbation of the spherical resonator. The inset shows the spectrum of the sphere for two different positions of the perturber.

During the experiments, the precise gap between the perturber and the resonator surface could not be determined *in-situ* with an optical microscope. A computational analysis was carried out to estimate this gap as described next.

Fig. 3.5a shows the calculated values of the integrand of equation (3.3) as a function of the azimuthal angle for  $d = 50$  nm. The resonator and perturber diameters used in the calculations correspond to those in the experiment. The results indicate that the region of interaction is limited to about  $\Delta\phi_0 = \pm 1.25^\circ$  for this case. Finally, the WGM shift as a function of  $d$  is calculated as shown in Fig. 3.5b by repeating the calculations of Fig 3.5a for a range of  $d$ . The maximum WGM shift of  $\Delta\lambda \approx 1.8$  pm obtained in the experiments (Fig. 3.4) indicates that the gap between the resonator and the perturber is  $d \approx 75$  nm.



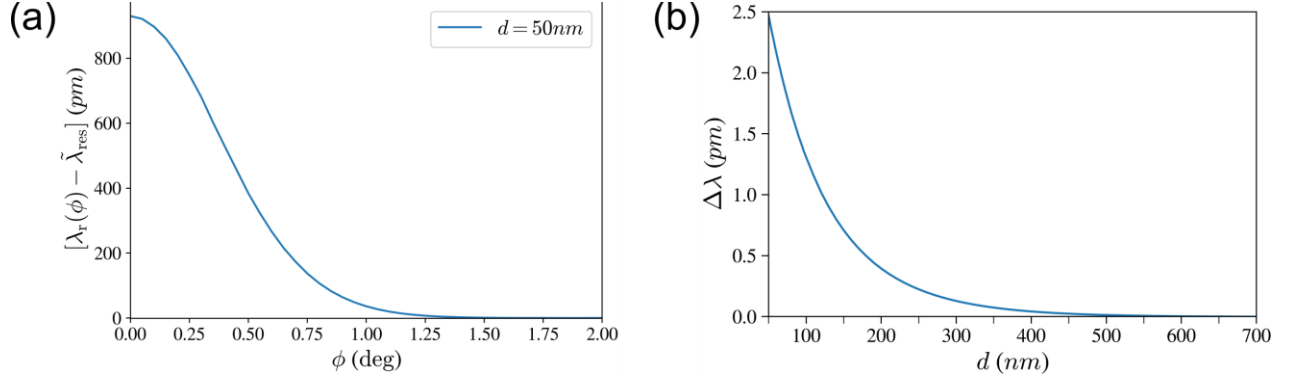


Figure 3.5: (a) WGM shift with azimuthal angle for  $d = 50$  nm. (b) WGM shift as a function of gap between the resonator and perturber. Each value in (b) corresponds to an integral of the curve in (a), using Eq. (3.3), for different gap values.

### 3.3.2. Ring Resonator

A cutaway view of the on-chip ring resonator is shown schematically in Fig. 3.6. The  $\text{Si}_3\text{N}_4$  ring resonator core has a nominal diameter of 24  $\mu\text{m}$  and a cross-section of  $7 \mu\text{m} \times 40$  nm. The  $\text{SiO}_2$  cladding layer is  $\sim 17 \mu\text{m}$  thick and sits on a 980  $\mu\text{m}$  thick Si substrate. The resonator core is positioned approximately 2  $\mu\text{m}$  below the top surface of the chip which is exposed to air. The bus carrying light in and out of the resonator (not shown in the figure) is positioned on the outer side of the resonator and has the same cross-section as the resonator. As depicted in Fig. 3.6, the perturber is on the top surface of the chip and moves along the radial,  $r$ -direction to interact with the evanescent field extending through the chip's top surface. The perturber is fabricated using the method previously described. The quality factor of the ring resonator is  $Q \sim 10^7$ .

A computational analysis is carried out as a first step to estimate the extent of the evanescent tail on the surface of the chip. Fig. 3.7 shows the variation of the normalized electric field magnitude in the radial,  $r$ , and surface-normal,  $z$ , directions. The parameter  $w = 7 \mu\text{m}$  is the width of the ring resonator and  $r_0$  is the radial distance to its mid-point as indicated in Fig. 3.6. The field is wider than the resonator width itself (Fig. Fig. 3.7a) and the maximum is only slightly off center due to the relatively large radius of the resonator. As seen in Fig. 3.7b, there is sufficient evanescent tail extension above the chip's surface to

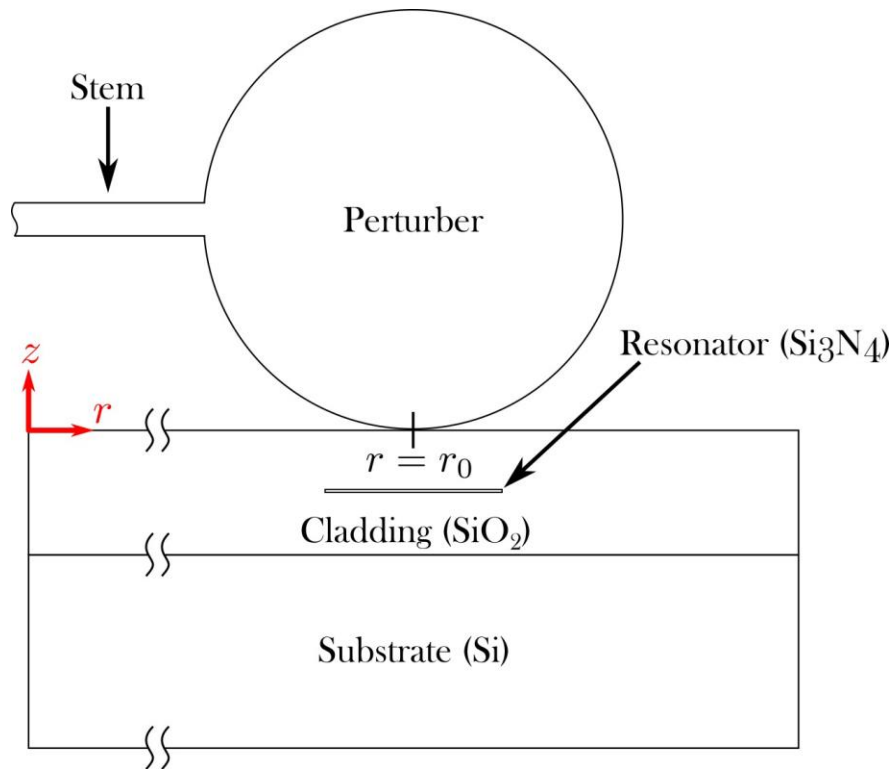


Figure 3.6: Cutaway representation of the on-chip ring resonator and perturber (not drawn to scale). Coordinates  $r$  and  $z$  are measured from the center of ring and chip's top surface.

interact with the perturber.

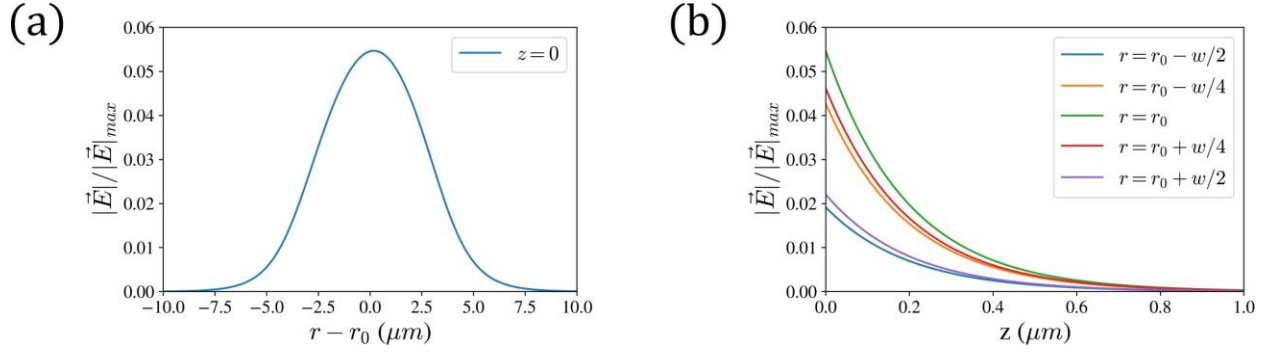


Figure 3.7: Normalized electric field magnitude: (a) Radial distribution along chip's surface; (b) Surface normal distribution. Since there is an evanescent tail extending past the chip's top surface, the modes of the ring resonator can be perturbed.

Fig. 3.8 is a photograph of the chip's top surface and the perturber placed over it. As indicated in the figure, the motion of the perturber is along the radial ( $r$ ) direction. The experimental result is shown in Fig. 3.9 along with the computational analysis using conditions approximating the experiment.

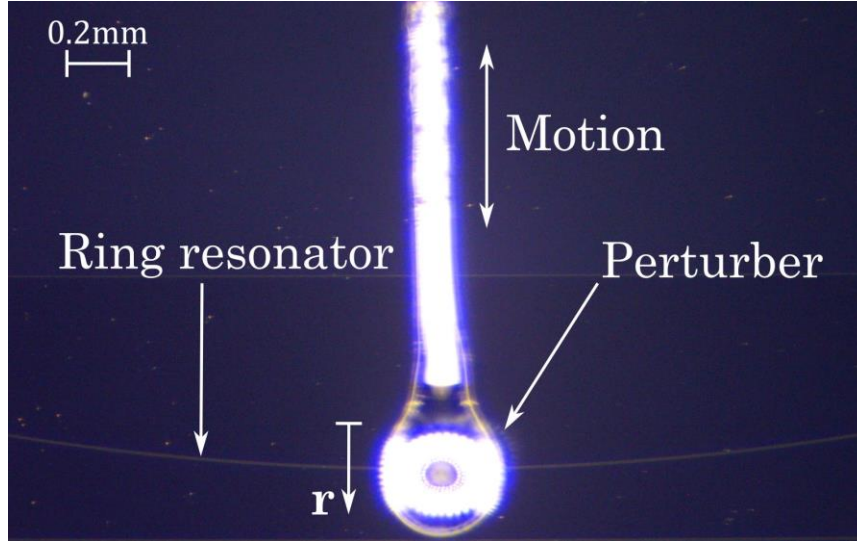


Figure 3.8: Photograph of the perturber and the ring resonator (top view).

The same approach as that for the sphere analysis is used except that in this case the sphere perturber is directly above the resonator as shown in Fig. 3.1. There is some dis-

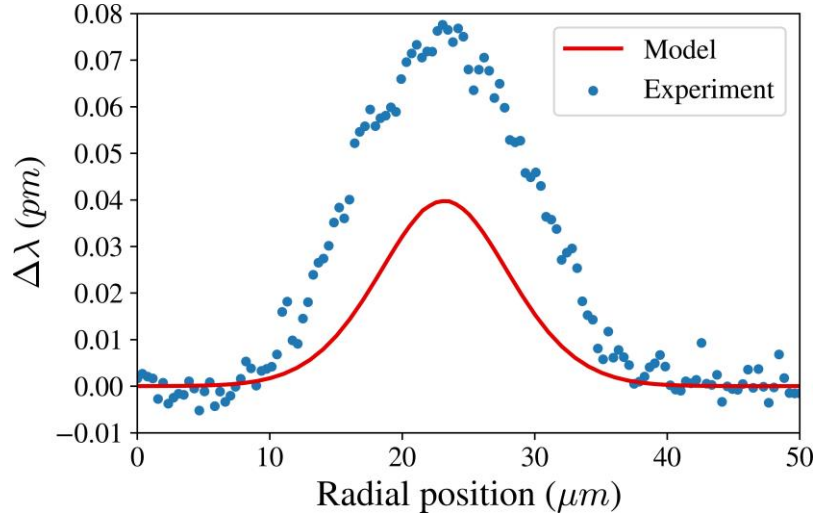


Figure 3.9: WGM shift versus perturber position. The computational curve is obtained using eq. (3.3) and the process described in fig. 3.5.

crepancy between the experimentally and computationally obtained WGM shift magnitudes. The difference in the magnitudes is possibly due to the non-spherical shape of the perturber in the experiment and the likely aberrations on the perturber's surface (the analysis assumes a perfect sphere with a smooth surface) resulting in a larger volume occupying the evanescent field. We do note, however, that the computationally and experimentally obtained WGM shift profiles agree well.

Overall, the results are encouraging as considerable WGM shifts are observed even when the cladding layer thickness above the resonator is significant. The retention of the cladding layer provides a level of protection of the resonator surface and its thickness can be optimized for a desired measurement sensitivity.

In the next experiment, a perturber, with a ferromagnet attached to its stem, is placed over the ring resonator to demonstrate a magnetic field detector concept. In this case, the perturber stem is aligned in a direction tangential to the ring resonator as shown in Fig. 3.10 and the stem's base is clamped at the edge of the resonator chip. The perturber material is SiO<sub>2</sub> and is fabricated in the same way as previously described. The ferromagnet is PDMS (10:1 base-to-curing agent ratio by volume) with iron dust mixed in before curing.

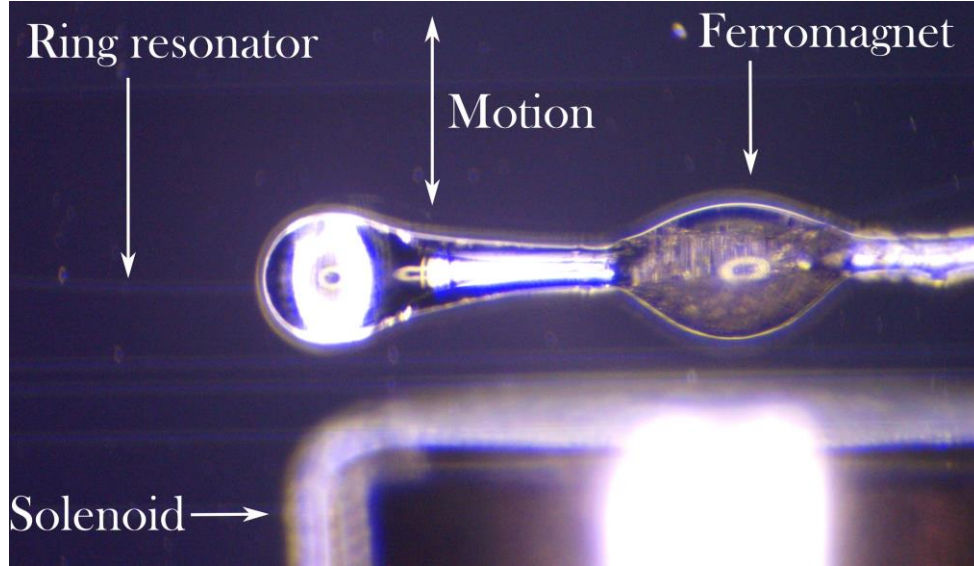


Figure 3.10: Photograph of magnetic field detection setup. The perturber sits on the top surface of chip. The solenoid generates a magnetic field that pulls the ferromagnet, causing the perturber to move across the evanescent field of the ring resonator.

A solenoid is placed approximately 1 mm away from the perturber. As the solenoid voltage increases, the induced magnetic field bends the perturber stem towards the solenoid, changing the tip position above the ring resonator, thereby causing a shift in the WGM. Before the solenoid is switched on, the tip of the perturber is located on the inner side of the ring resonator (hence, outside of its evanescent field).

Figure 3.11 shows the WGM shift as a function of the magnetic field strength. Fig. 3.11a is the result for a single sweep of the solenoid voltage. In the graph, each data point corresponds to the WGM shift obtained from a single scan of the laser wavelength. The laser is scanned at a repetition rate of 400 Hz and the waveform is sinusoidal. Therefore, each data point in Fig. 3.11a represents a measurement time resolution of 2.5 ms. These transient measurements exhibit some random noise (primarily electronic and photon shot noise). Fig. 3.11b is the average of 20 such individual realizations for each data point removing much of the random noise. As the magnetic field strength increases, the perturber moves over the resonator interacting with its evanescent tail until the magnetic field is strong enough to move it completely outside of the resonator on the outer side of the ring. Although

the magnetic field sensitivity in these measurements is modest, the results demonstrate the viability of evanescent field perturbation for sensor applications.

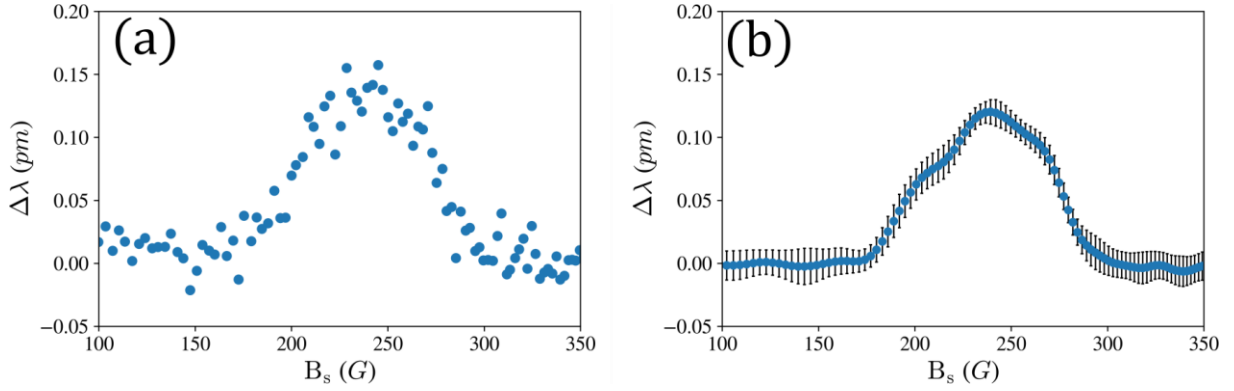


Figure 3.11: WGM shift versus magnetic field. (a) Single realization - each data point corresponds to one laser scan at a rate of 400 Hz. (b) Averaged measurement for 20 realizations with standard deviation for each magnetic field value shown as error bars.

The ring resonator results show that even with a cladding layer of considerable thickness ( $\sim 2 \mu\text{m}$ ) above the resonator, the dielectric perturber still induces a significant amount of shift in the resonator's WGM. The present magnetic field sensing experiment yields a measurement sensitivity of  $1.74 \times 10^{-3} \text{ pm/gauss}$ . For a resonator with  $Q = 10^7$  and a WGM shift measurement resolution corresponding to 1% of the FWHM of the resonance linewidth [19], the detection resolution is  $\approx 0.753 \text{ gauss}$ . The measurement sensitivity of the system can be optimized by varying several parameters including the resonator and perturber material, resonator shape and size, perturber stem length and diameter and the thickness of the cladding layer.

### 3.4. Future Considerations

The results presented in this chapter demonstrate the concept of an evanescent field sensor that can be configured to measure quantities such as displacement and magnetic field. This preliminary analysis assesses the feasibility of a reliable and controllable perturbation of the optical modes of different resonator geometries. For a robust sensor, integrated resonators, such as the ring employed here, are best suited for practical real-world applications. The

flexibility of the proposed approach allows for either a detached or an integrated perturber. In the former, more freedom is possible in the design of the perturbing geometry but that would likely require an extensive and careful calibration process. Additionally, robustness is not guaranteed as the perturber could be displaced beyond the sensing range of the resonator.

A monolithic sensing element, where the perturber is fully integrated and built as part of the microfabrication process along with the resonator, can provide a highly robust sensor configuration. For instance, in chapter 2, the sensitivity of the seismometer is primarily limited by the stiffness of the substrate. While a thin substrate can be used to reach higher sensitivities, the high temperature processes used in the resonator fabrication pose a risk to the structural integrity of the substrate (i.e., silicon wafer) due to thermal stress caused by the deposition of different films. An alternative to the approach described in chapter 2, is to build a thin perturber on top of the resonator such that its geometry allows for measurement of low frequency vibrations. The perturber can be a thin plate hovering above the resonator inside the evanescent field. Fig. 3.12 shows an example of a geometry that can be used to estimate acceleration based on proximity effect.

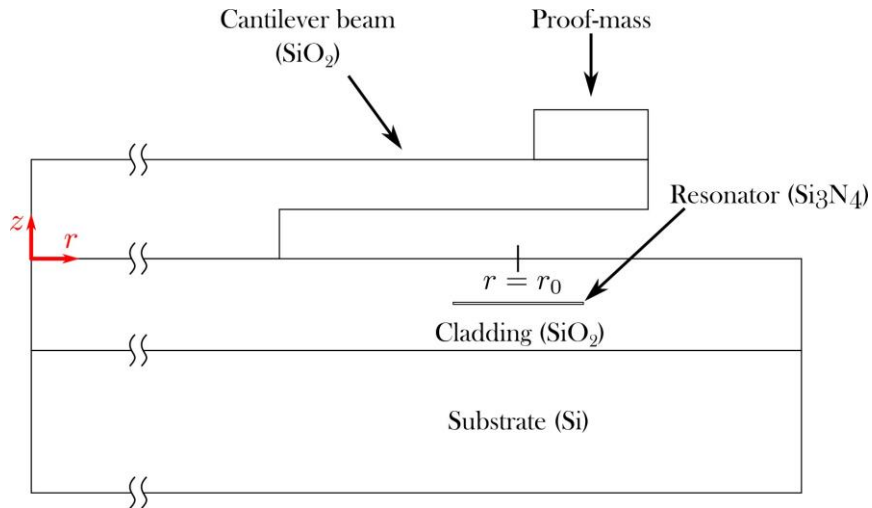


Figure 3.12: Example of on-chip ring resonator with a built-in perturber (cantilever beam).

In addition to WGM shift, the perturbation of the evanescent tail also alters the optical Q-factor of the resonator. Fig. 3.13 shows both the WGM shift and Q of the ring resonator

as it interacts with the ferromagnetic perturber. In the magnetic field experiment the  $Q$  is dynamically adjusted from an initial value of  $\sim 1 \times 10^7$  to  $0.75 \times 10^7$ . The modulation of the resonator's  $Q$  is useful in applications where a dynamic optical filter with adjustable frequency and linewidth is required. If combined with electro-optic or thermal modulation of the ring's resonance, the evanescent tail perturbation can be used to create a filter with real-time adjustable frequency and linewidth.

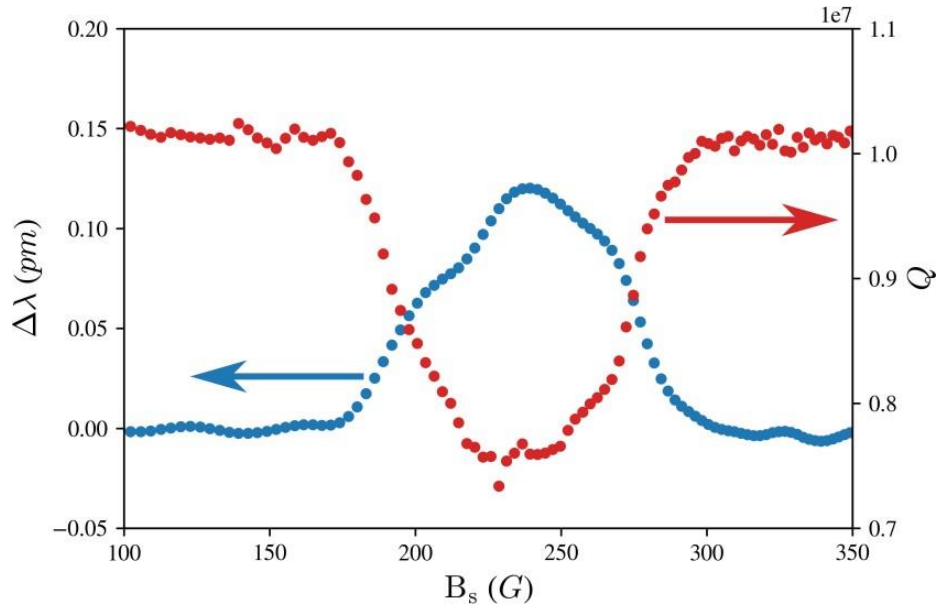


Figure 3.13: Mode shift and  $Q$ -factor of ring resonator as the perturber interacts with the evanescent tail. The  $Q$ -factor is modulated by the interaction between the perturber and ring resonator.



## Chapter 4

### Self-Referencing WGM-based Doppler Sensor

The sensor concepts presented thus far rely on the morphology change of the WGM resonator, eq. (1.2), to induce a mode shift. This chapter discusses an additional WGM application, namely the Doppler shift detector in which the morphology of the resonator is not intentionally modified. A scanning laser light is directed to a moving solid surface or a transparent gas and the reflected (or scattered) light from the target is passed through the WGM resonator to detect the Doppler shift due to the relative motion between the target and the sensor. The approach may find application in a range of areas including surface vibration and fluid flow measurement. WGM sensors that operate based on the Doppler effect have been demonstrated to measure the velocity of a rotating disk [60] and a water droplet-seeded free air jet [50] using a sphere and an integrated ring resonator, respectively. In these studies, the WGM resonator acts as a stable wavelength shift indicator in the optical spectrum of laser light.

A challenging aspect of WGM sensing is the influence of environmental conditions (temperature, pressure, humidity, etc.) on the resonator morphology due to thermal and mechanical effects such as thermorefractive and thermoelastic fluctuations, thermal expansion [51], and deformation of the resonator caused by variations in the ambient pressure and background acoustic noise [35]. Additionally, due to variations in the ambient temperature, the laser output power and wavelength may drift even when a thermoelectric control unit is utilized. All these effects are observed as unwanted and uncontrolled drift in the WGM.

A secondary resonator can be used to account for the undesirable influences of the environment on the measured signal [50]. This approach requires separate calibrations of the sensing and reference resonators, and since two distinct optical cavities are employed, their response to external perturbations is not assured to be the same. Furthermore, the two

resonators' distinct intrinsic thermodynamic noise constitutes an additional source of measurement uncertainty. In this chapter, a robust sensor concept that relies on a single resonator to generate both the sensing and reference WGM signals is presented. This configuration can potentially eliminate WGM drift effect due to changes in environmental conditions.

#### 4.1. Sensor Concept

Doppler effect refers to the shift in wavelength due to the motion of a wave emitting source relative to a receiver. For an optical system, the magnitude of the Doppler shift ( $\Delta\lambda_D$ ) is related to the target's velocity by [44]:

$$\frac{\Delta\lambda_D}{\lambda} = \frac{\vec{V} \cdot (\vec{k}_r - \vec{k}_i)}{c}, \quad (4.1)$$

where,  $\vec{V} \cdot (\vec{k}_r - \vec{k}_i)$  is the projection of the target's velocity onto the bisector of the unit vectors representing the incident ( $\vec{k}_i$ ) and reflected ( $\vec{k}_r$ ) beams, and  $c$  is the speed of light.

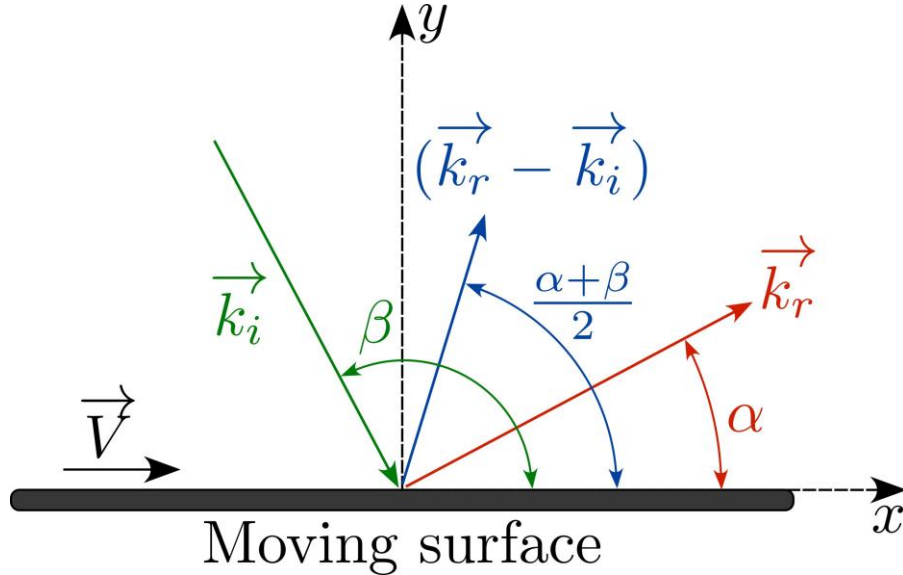


Figure 4.1: Schematic representation of Doppler effect for a uniformly moving surface.

For a uniformly moving reflective surface the projected velocity can be determined using the illustration provided in figure 4.1. Light transmitted by a fixed lens is incident upon a moving target, which in turn reflects the light to a collection lens. The bisector can be

defined as

$$\vec{k}_r - \vec{k}_i = 2 \cos \frac{\alpha - \beta}{2} \cos \frac{\alpha + \beta}{2} \hat{x} + \sin \frac{\alpha + \beta}{2} \hat{y} . \quad (4.2)$$

One immediate observation is that for mirror reflection,  $\alpha$  and  $\beta$  are supplementary angles (i.e.,  $\alpha + \beta = \pi$ ) and the bisector becomes perpendicular to  $\vec{V}$  ( $= v \hat{x}$ ), resulting in zero Doppler shift. In the case of retro-reflection (i.e.,  $\alpha = \beta$ ), as shown in Fig. 4.2, the bisector becomes  $2 [\cos(\alpha) \hat{x} + \sin(\alpha) \hat{y}]$ , leading to

$$\frac{\Delta\lambda_D}{\lambda} = \frac{2v}{c} \cos(\alpha). \quad (4.3)$$

In the current sensor, the Doppler shift,  $\Delta\lambda_D$ , is observed as a shift of the WGM allowing for direct calculation of the target's velocity.

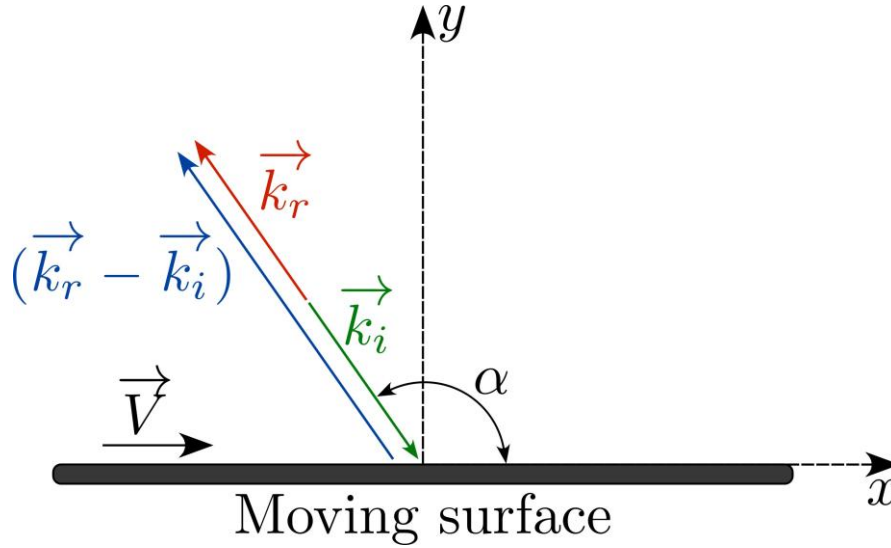


Figure 4.2: Optical wave vectors for a retro-reflective surface.

The moving target illustrated in Fig. 4.1 can either be a scatterer (e.g., aerosols, gas molecules) or a reflecting surface (e.g., mirror, retroreflective material). Conceptually, the functioning of the sensor is the same regardless of the nature of the target. However, the intensity of the back-reflected light and its linewidth changes significantly depending on the application. Reflected light from a solid surface is much stronger (typically more than one order of magnitude) than scattered light from aerosol particles in a gas flow (which depends

on the size and refractive index of the particles) [49]. Also, the linewidth of the collected light from a solid surface is the same as that of the incident laser light. In the case of non-aerosol, pure gas flows, where the scattering is from gas molecules themselves (for example in the Rayleigh or Rayleigh-Brillouin regime) the intensity of the scattered light is yet a few orders magnitude smaller than that from seed particles and exhibits thermal broadening.

Therefore, in the case of gas molecular measurements, higher power laser sources and extended integration times would be required to accumulate sufficiently large number of photons on the detector for acceptable levels of signal-to-noise ratios. In addition to high intensity, reflective solid surfaces (e.g., mirrors) provide very stable and robust optical coupling with a simple apparatus. For these reasons, a retro-reflective surface is selected as the moving target for a proof-of-concept in the present study.

#### **4.2. Optoelectronic Configuration**

Figure 4.4 is a schematic representation of the self-referencing sensor system. The waveform generator modulates the 1313 nm DFB laser wavelength similar to the system described in Fig. 2.1. The polarization of the light is adjusted using the polarization rotator. The optimal polarization state maximizes the intensity of the transverse electric (TE) modes of the waveguide. The light is then divided into two by a 90:10 splitter. The photodiode, PD1, output signal from the 10% light (designated by cyan color in the figure) is used to normalize the intensity of the photodiode outputs of PD2 and PD3.

A second 90:10 fiber splitter on the 90% side divides the laser light into two as shown. One side (blue) is directly sent to the resonator and terminated at PD2 on the output side after passing through an optical circulator. When the laser is tuned across a narrow wavelength range, the WGM dips are observed by PD2 as shown (blue). This is the reference WGM signal. The other side (green) is coupled to a collimating lensed fiber and directed to the targeted measurement location. The reflected light from the target surface is collected by the same collimating lensed fiber (red). Due to the motion of the reflector, this light is Doppler shifted. The shifted light is directed to the resonator and the WGM is seen as a dip at PD3

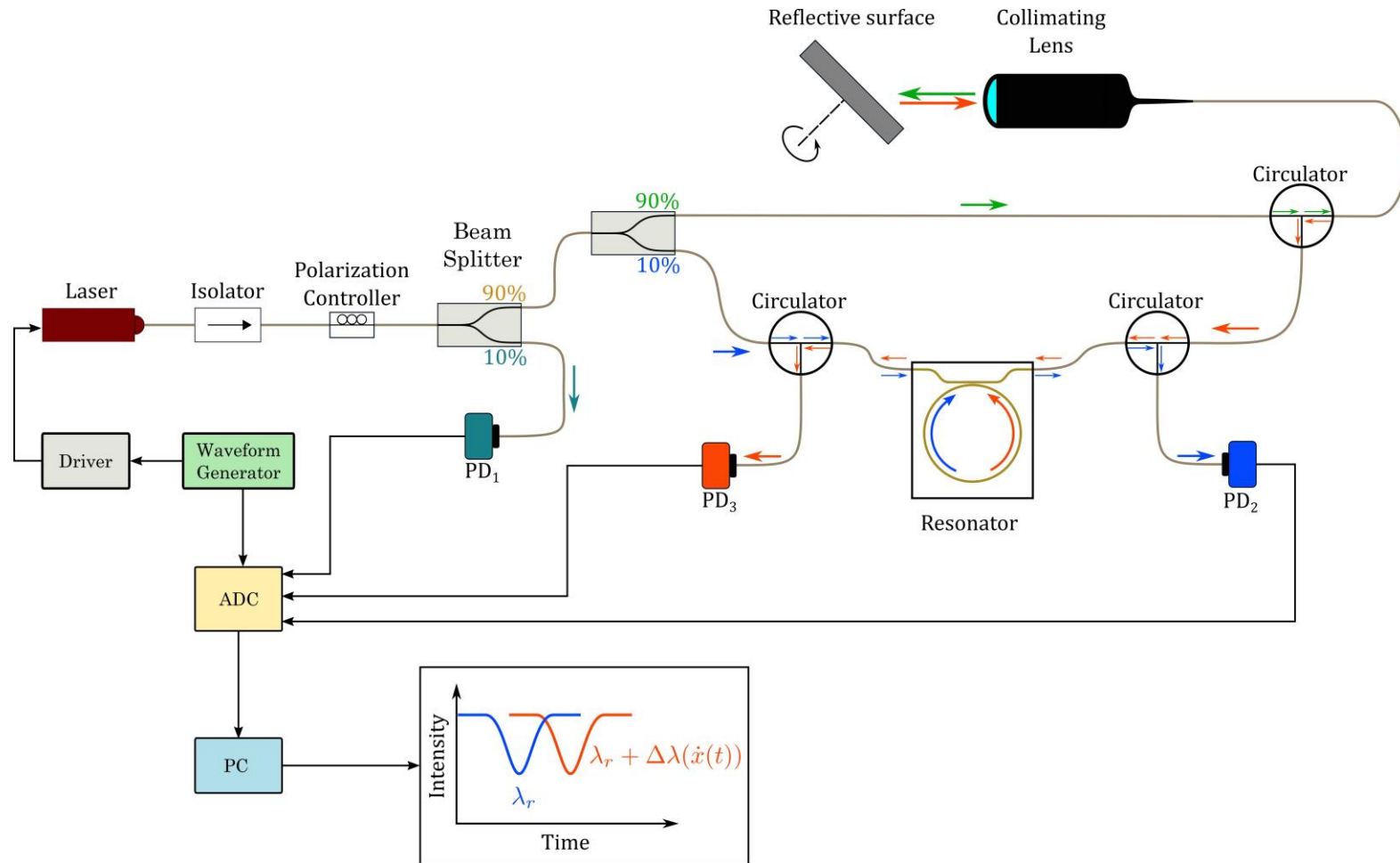


Figure 4.3: Opto-electronic configuration of the self-referencing WGM-based Doppler sensor.

as shown (red). The relative shift,  $\Delta\lambda_D$ , between the blue dip and the red dip is the true Doppler shift, clear of any drift effects due to environmental conditions. It is a measure of the velocity of the interrogated surface at time,  $t$ . The data acquisition and signal processing are performed as described in 2.2.1.

### 4.3. Measurement Technique

Figure 4.4 illustrates the concept of Doppler shift calculation using WGMs excited by a tunable laser modulated by a ramp waveform over a certain time period. Since the morphology of the resonator is not intentionally modulated, the reference and sensing resonances correspond to the same resonant wavelength (eq. 1.1), as indicated by the horizontal dashed black line. However, due to the wavelength shift of the reflected light, the WGMs are observed at a different point in the cycle of the laser scan. The temporal displacement of the resonance determines the Doppler shift according to

$$\Delta\lambda_D = -\Delta V \frac{\lambda}{V}, \quad (4.4)$$

where  $\lambda/V$  relates the laser driver voltage to the wavelength of the laser light, and  $\Delta V$  is the Doppler shift in terms of the driving voltage. The negative sign is included because a redshift creates an apparent decrease of the WGM's resonant wavelength, as depicted in figure 4.4.

### 4.4. Experimental Setup

The photographs in figure 4.5 show the configuration used to demonstrate the concept of a WGM-based, self-referencing velocimeter. A DC motor rotates the disk to which the retro-reflective tape is attached. The rotation of the disk generates a constant planar velocity of the tape, leading to the condition illustrated in figure 4.2. The reflective material has glass beads that couples the light from the lens back into itself. The fiber-pigtailed collimating lens is aligned to the tape such that the intensity of the reflected light is at its maximum. The angle ( $\alpha$ ) between the lens and the disk is  $35.62^\circ$ , corresponding to  $\sim 81\%$  of the maximum

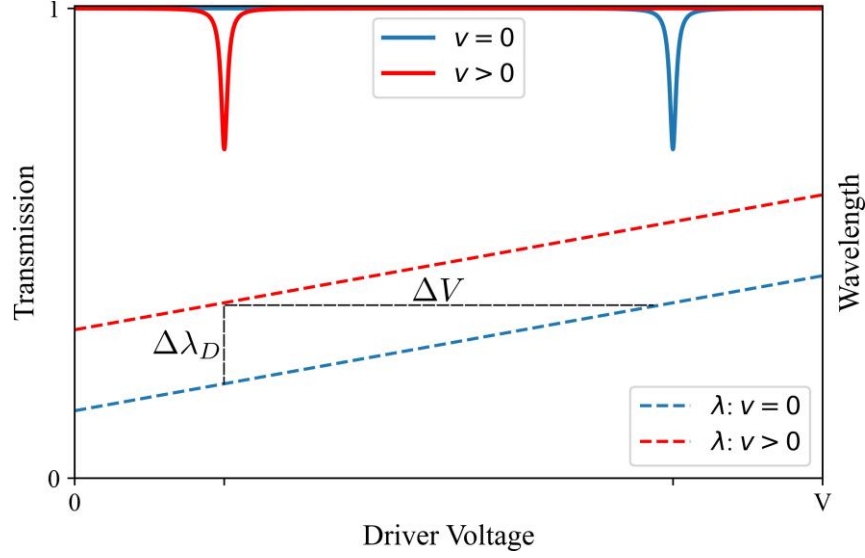


Figure 4.4: Illustration of measurement technique. The dashed lines correspond to the wavelength of the input light before (blue) and after (red) a Doppler shift is introduced. The solid lines are the spectrum of a ring resonator measured by the original laser light (blue) and the Doppler shifted light (red).

Doppler shift ( $\alpha = 0$ ). The optical fiber is connected to an optical circulator, and the rest of the system is arranged as depicted in figure 4.3.

The reflective tape provides the means to measure the rotational speed of the disk, hence, the linear (tangential) velocity at the location where the light is focused. As the disk rotates, the tape moves away from the focus point, resulting in mirror reflection of the light and loss of signal in PD3 (Fig. 4.5). The repetition rate of coupling/uncoupling determines the rotational speed of the disk.

Three approaches can be employed to estimate the Doppler shift. In the first, the laser is scanned slower than the disk and the WGM profile is sampled over the reflecting/nonreflecting cycles of the tape. The benefit of this approach is that at slow scanning (tuning) rates the laser follows the driving signal avoiding distortion of the laser's tuning waveform, with a negligible phase and no reduction in amplitude. The downside of this method is that the post-processing analysis becomes challenging as the WGM must be reconstructed individually.

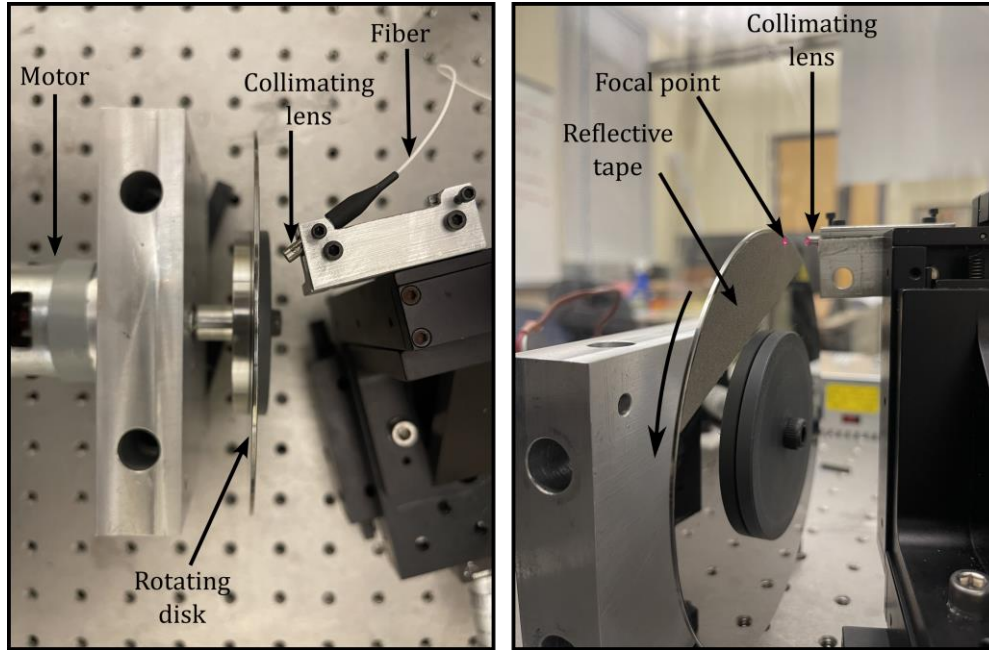


Figure 4.5: Top (left) and side (right) views of experimental apparatus. In the side view a red-light alignment laser is used to indicate the focal point of the lens.

In the second technique, the laser's wavelength modulation is harmonic (sine wave) and tuning rate is faster than the rotation of the disk. The laser must be scanned multiple times within a single cycle of the disk to allow for reliable measurements. This leads to scanning rates in the order of 1-10 kHz for disk speeds between 150-350 Hz. The main advantage of this method is that the WGM is fully sampled various times in one disk cycle and the determination of the Doppler shift is straightforward. On the other hand, at such high rates the output of the laser is distorted (i.e., amplitude reduction and phase delay) with respect to the driving harmonic signal due to the thermal inertia of the internal laser's system. Therefore, a correction of the measured WGM shift is required based on the dynamic calibration of the laser, as described in [1].

The third method consists of a gradual adjustment of a DC voltage applied to the laser. The DC signal has a stair-step profile over time and each value of the applied voltage, and laser wavelength, is maintained long enough for the rotating disk to complete at least two rotations. The advantage of this method is that the step-stair profile allows for flexibility



in the sampling of the WGMs. For example, certain portions of the optical spectrum that require higher resolution can be finely resolved by making the corresponding step change smaller. However, the primary drawback is that both the driver and the laser need time to reach the desired wavelength, typically 10 ms, which can be a limiting factor depending on the application.

Compared to the previously described methods, the stair-step is more suitable for the current experiment because, although the disk will rotate at a constant rate, the intensity of the Doppler shifted light is expected to vary due to wobbling and different size scatterers (i.e., glass beads in the retro-reflective tape) exiting and entering the collection region. By holding the wavelength constant, the variations in the signal intensity are averaged out, reducing the noise and uncertainty for each sampled point in the WGM's spectrum. For these reasons, the stair-step driving signal is preferred over the other two methods to provide a qualitative assessment of the efficacy and feasibility of the self-referencing sensor concept.

#### **4.5. Results**

The resonator and waveguide are embedded in a silicon-on-insulator fiber-pigtailed chip. The ring has a cross-section of  $480 \text{ nm} \times 220 \text{ nm}$  ( $W \times H$ ) and a radius of  $11.25 \text{ }\mu\text{m}$ . The characterization of the resonances at  $1.3 \text{ }\mu\text{m}$  laser wavelength yields Q-factors of  $\sim 1 \times 10^5$  in both directions as shown in figure 4.6. These two resonances are used to calculate the Doppler shift by employing a Lorentzian fit (LF) algorithm, which considers the whole WGM profile instead of just the location of the dip minimum.

The rotational speed of the disk is adjusted by controlling the voltage of the motor driver. Here, the selected input motor voltage ranges from 2 to 20 V with a 2 V step, corresponding to rotational speeds of  $\sim 30\text{-}360 \text{ Hz}$ . For each motor voltage, the WGMs are sampled with a stair-step and the LF algorithm tracks their location. Figure 4.7 shows the fitting of a Lorentzian to identify the location of the sensing WGM relative to the respective reference one for different speeds.

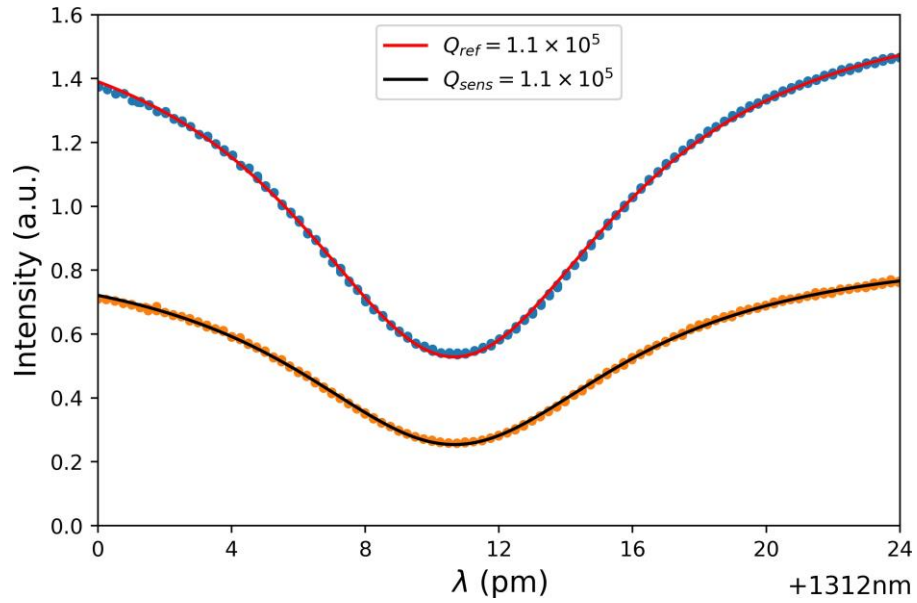


Figure 4.6: Characterization of resonances in the two propagation directions: (orange) from disk (counter-clockwise rotation) and (blue) from laser (clockwise rotation) - see Fig. 4.3. The solid lines are the Lorentzian fitting for each WGM.

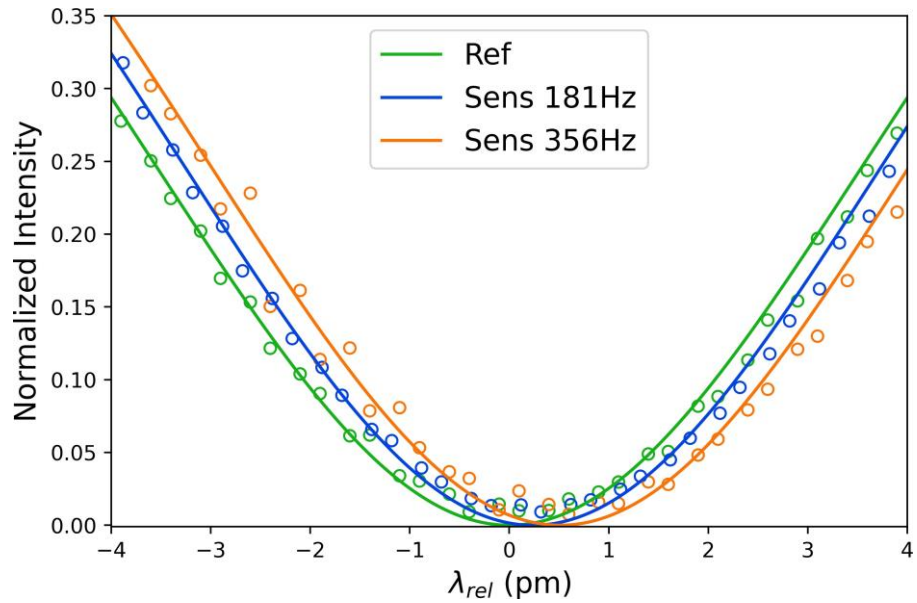


Figure 4.7: Sensing resonance for two different rotational speeds. The x-axis is offset by the location of the reference resonance.

The process shown in Fig. 4.7 is repeated for various rotation rates. The measured Doppler shift between the sensing and referencing WGMs as function of the disk speed is shown in fig. 4.8, alongside a best fitted line. In accordance with eq. (4.3), the measured Doppler has a linear relationship with the disk speed. The best fit line has a slope of 1.48 fm/Hz with an RMSE of 7.35 fm, corresponding to  $\sim \delta\lambda/1700$  for a Q of  $1.1 \times 10^5$  and an operating wavelength of 1312 nm. It is important to note that the sensing and reference WGMs exhibited thermal drift but thanks to the dynamic referencing signal originating from the same resonator, the measured shift is not affected by thermally induced fluctuations.

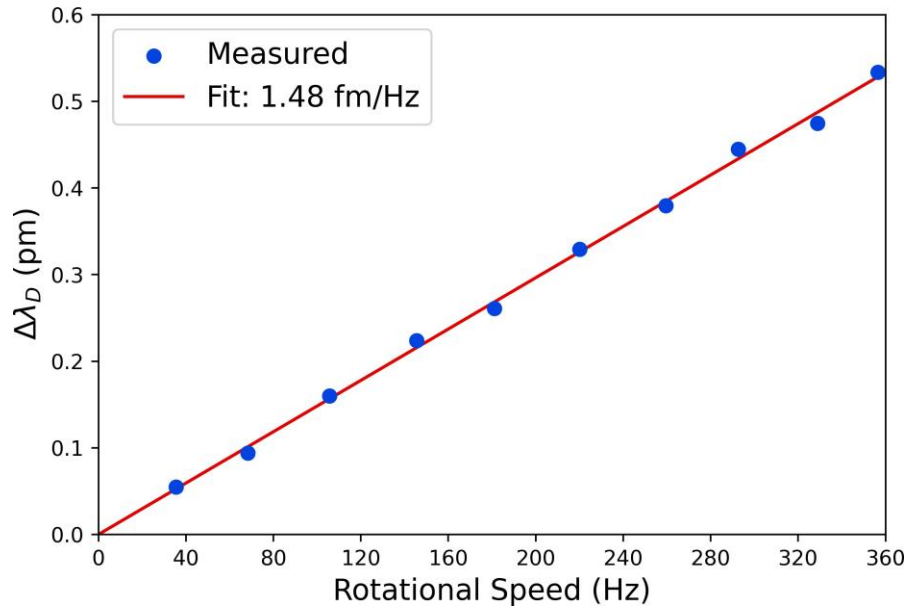


Figure 4.8: Measured Doppler shift and best fit line as a function of angular velocity.

The results suggest that the present configuration is capable of estimating shifts significantly smaller than the linewidth of the resonance. In the experiment the smallest measured Doppler shift, at 35.47 Hz, is 54.80 fm, equivalent to  $1/217^{\text{th}}$  of  $\delta\lambda$  – often taken as the limit of detection. In practice, the thermo-refractive noise usually represents the limit of detection and for Si ring resonators, such as the one employed here, it is in the order of 10 fm [11]. Assuming that the thermo-refractive noise model is an accurate estimation of the noise-floor, the shifts measured here are close to the resonator’s theoretical thermodynamic limit. However, for a sensing configuration capable of measuring shifts in the order of the thermore-

fractive noise needs to overcome the noise introduced by the electronics (e.g., photodetectors and A/D). The significance of the current study is that the self-referencing sensing scheme presented here extends the capability of WGM resonators beyond their established limit of detection.

#### **4.6. Future Considerations**

The Si resonator employed in this section has a small footprint, making it highly susceptible to variations in temperature due to the lack of thermal inertia. Therefore, monitoring of the WGM shift for extended periods of time proved to be challenging as the WGM quickly drifted out of the measurement window. To reduce thermal drift, larger resonators will be used in future studies, such as the one utilized in chapters [2](#) and [3](#). Furthermore, a characterization of the resonator's noise-floor must be carried out to effectively determine whether the self-referencing concept bypasses the noise in the measurements introduced by the laser and the resonator.

Resonators with a larger footprint can offer higher  $Q$ 's than the current ring. Waveguides made of  $\text{Si}_3\text{N}_4$  on  $\text{SiO}_2$  have been attracting significant interest and offer  $Q$ 's exceeding  $10^7$  [[20](#)] that can further extend the capabilities of the self-referencing sensor concept. High  $Q$ s allow for better sensing resolution since they reduce the required laser scanning range to fully resolve the WGMs.

In future studies, the goal will be to assess the limitations of the current sensing scheme. The goal will be to demonstrate detection of velocities smaller than 1 m/s and hopefully achieve a measurement resolution that can make this sensor concept suitable for field deployment in applications such as vibrometry, flow velocimetry, and seismometry.

## Chapter 5

### Conclusion

This dissertation demonstrates the application of micro-ring-based WGM sensors using three distinct concepts. The work presented highlights the feasibility and versatility of integrated resonators to measure a number of parameters including acceleration/seismicity, displacement, magnetic field and velocity, based on mechanical deformation (strain) principles, evanescent field perturbation, and Doppler effect, respectively. The effort presented here aims to be the necessary spark that leads to the development and deployment of rugged, passive, robust, and reliable photonic integrated circuit based WGM sensors.

Chapter 2 demonstrates the concept of an all-optical cantilever-based seismometer that employs an integrated ring resonator. The acceleration of the base is determined by the WGM shift of the resonator embedded in a chip. The sensor's system parameters are estimated by observing the free vibration of the system through the WGM shift. The prototype developed and tested in this study uses a relatively thick Si substrate and therefore is limited in its sensitivity to about  $2 \text{ pm}/(\text{m/s}^2)$ . The sensitivity can be improved by using thinner substrates or softer "chip" material at the expense of bandwidth. For long-period seismometers a narrow-bandwidth is a desirable trait since the higher frequency seismic noise does not factor into the collected data. On the other hand, certain applications may require a broad-band response and high sensitivity (typically addressed by broad-band seismometer that incorporate a force feed-back mechanism) and simply adjusting the thickness and material of the substrate might not be enough to achieve the desired performance – in which case novel optical techniques can be devised.

The work carried out to develop the prototype photonic seismometer is mainly motivated by the need for rugged, small size, weight and power consumption (SWaP) seismic sensors for the exploration of Jupiter's moon, Europa. Europa is speculated to have a liquid ocean

underneath its icy surface. The low temperatures pose a challenge for any instrument deployed on Europa's surface, thus, an alternative to traditional sensors must be considered. In the next iteration of the photonic seismometer project, the primary goal will likely be to assess its performance at cryogenic conditions. If successful, the proposed passive (no force feedback) seismic sensor would become a strong candidate for future planetary exploration.

The prototype of this work serves as a proof-of-concept, demonstrating the feasibility of a photonic integrated circuit-based seismometer embedded in a silicon chip. It is hoped that the current work will pave the way for follow up investigations of chip-based photonic seismometers with improved optomechanical performance. The ultimate goal of is the development of sensors that can be used in both planetary and Earth-bound applications with minor design changes. The chip-based seismometer presented here can be fabricated in large batches inexpensively using modern micro-fabrication technologies, such as lithography. This allows for the fabrication and deployment of networks of sensors connected to a single (or only a small number of) attending electro-optic unit (with the input laser, photodetectors and electronic circuits) via optical fibers. Further, the networks can be spread out over extended physical areas with the attending electro-optic unit placed at large standoff distances.

Chapter 3 explores the concept of a mechanical sensor based on the perturbation of the evanescent field of an integrated ring resonator. The approach requires that the resonator's evanescent tail extends past the outer surface. Longer evanescent tails allow for higher measurement resolution. The experiments and analyses show that the evanescent field on the outer surface of a dielectric resonator can be perturbed in a well-controlled manner using a bulbous-tipped dielectric stem to induce WGM shifts. The results demonstrate the feasibility of a perturber-coupled sensor approach for both sphere (or similar, three-dimensional geometry) and planar, on-chip resonators. Although a ring-resonator is employed here for the planar sensor approach, the technique would be effective with other geometries, such as disks or racetrack configurations. The method presented here provides an attractive alternative to sensors that depend on the modification of the morphology of the resonator itself.

The ring resonator results show that even with a cladding layer of considerable thickness ( $\sim 2 \mu\text{m}$ ) above the resonator, the dielectric perturber still induces a significant shift in the resonator's WGM. The present magnetic field sensing experiment yields a measurement sensitivity of  $1.74 \times 10^{-3} \text{ pm/gauss}$ . For a resonator with  $Q = 10^7$  and a WGM shift measurement resolution corresponding to 1% of the FWHM of the resonance linewidth, the detection resolution is  $\sim 0.75 \text{ gauss}$ . The measurement sensitivity of the system can be optimized by varying several parameters, including the resonator and perturber material, resonator shape and size, perturber stem length and diameter, and the thickness of the cladding layer.

The envisioned evanescent field-based sensor will be a monolithic structure. Integrating the perturber into the optical chip would make the measurement system rugged to external environmental effects and provide a reliable and consistent interaction with the optical mode. The integration can be achieved by employing microfabrication processes to build the perturber above the resonator. The concept can be extended to sensing different quantities such as displacement, magnetic field, and seismic activity (acceleration). Additionally, evanescent field perturbation provides a means to modify the linewidth (Q-factor) of the WGM, in addition to the shift, which can prove useful for applications where the resonator is used as a dynamic filter. Combining the linewidth adjustment with the other modulation effects (e.g., electro-optic) would yield an effective and highly controllable optical filter that can be used in, for example, spectroscopy.

Chapter 4 investigates the concept of a microresonator-based self-referencing Doppler sensor. Such sensors can be used, for example, as velocimetry in transparent fluids or as solid surface vibrometry. The experiments show that a single ring resonator can be used effectively to generate a reference and sensing signal originating from the same light source (i.e., laser). In the present demonstration experiments, the sensing signal is obtained by directing the laser light on a rotating disk and collecting the reflected light with the Doppler shift. Passing the reference and sensing light through the same waveguide-coupled ring resonator, moving in opposite directions, generates two distinct signals. The relative displacement between the

two WGMs determines the Doppler shift (and hence, velocity) eliminating the effect of laser frequency or resonator mode drifts due to external effects (primarily temperature).

The results indicate a consistent measurement of the disk velocity using the Doppler shift thanks to the reference signal that provides a dynamic offset to correct for possible thermal drifts that can affect both the laser cavity and the ring resonator. The preliminary experiment demonstrates that a single resonator can be used for a self-correcting Doppler sensor that does not necessitate an active component such as a frequency shifter present in traditional laser Doppler velocimeters or vibrometers.

The effectiveness (and the resolution) of the proposed self-referencing Doppler sensor depends on the optical quality factor,  $Q$ , of the resonators. The research carried out here envisions using high- $Q$  resonators in the order of  $\geq 10^7$ . One of the challenges encountered in the experiment described in Chapter 4 is associated with the moderate  $Q$  ( $\sim 1 \times 10^5$ ) of the 11.25  $\mu\text{m}$  radius silicon resonator that was available for the experiment. The linewidth of the resonance is approximately one order of magnitude larger than the maximum Doppler shift ( $\sim 1$  pm) provided by the rotating disk. The relatively large linewidth of the resonance limits the detection of small Doppler shifts (and the corresponding velocities). Employing a high- $Q$  resonator, such as the one used in Chapters chapters 2 and 3 ( $Q \sim 10^7$ ), will allow for the direct detection of Doppler shifts corresponding to 1 m/s or smaller. Unfortunately, those larger size ring resonators were not available for the research of Chapter 4.

Silicon waveguides and resonators have been reported to exhibit significant back-reflected light due to the refractive index contrast between the silicon core and the oxide cladding. This was also experienced in the present study. The reflected light deteriorates the quality of the signals and interferes with the measurement. Thanks to the low contrast between core and cladding, silicon nitride waveguides and resonators exhibit little or no back-reflection. With more suitable resonators, the goal will be to develop a minimalistic sensing scheme that could potentially use a single detector to demonstrate a very-low noise self-referencing WGM-based Doppler sensor. They would enable more efficient utilization of a ring-couple waveguide's bidirectionality.



This dissertation demonstrates three distinct sensor concepts that rely on integrated ring resonators. The ultimate goal is to develop and build photonic sensors that can be readily deployed in the field. Thus, future work may include efforts to improve these concepts further that lead to packaged sensors. Future work will also likely include the development of robust and low noise detection schemes with the aim of delivering performances similar to or better than traditional devices while remaining passive with superior SWaP.

## BIBLIOGRAPHY

- [1] Ali, A. R. *Dielectric micro-resonator-based opto-mechanical systems for sensing applications*. PhD thesis, Southern Methodist University, 2015. [55](#)
- [2] Ali, A. R., Ötügen, V., and Ioppolo, T. High data rate transient sensing using dielectric micro-resonator. *Applied optics* 54, 23 (2015), 7076–7081. [18](#), [20](#)
- [3] Baloch, S., Ghazali, F., Mir, N., Farrukh, F., Ismail, H., and Qadri, M. Y. Hardware realization of locally normalized cross correlation algorithm. In *The 2014 2nd International Conference on Systems and Informatics (ICSAI 2014)* (2014), IEEE, pp. 378–382. [20](#)
- [4] Bao, M., and Yang, H. Squeeze film air damping in mems. *Sensors and Actuators A: Physical* 136, 1 (2007), 3–27. [29](#)
- [5] Berger, J., Davis, P., Widmer-Schmidrig, R., and Zumberge, M. Performance of an optical seismometer from 1  $\mu$ hz to 10 hz. *Bulletin of the Seismological Society of America* 104, 5 (2014), 2422–2429. [8](#)
- [6] Bernard, P., Feron, R., Plantier, G., Nercessian, A., Couteau, J., Sourice, A., Feuillo, M., Cattoen, M., Seat, H.-c., Chawah, P., et al. Onland and offshore extrinsic fabry–pérot optical seismometer at the end of a long fiber. *Seismological Research Letters* 90, 6 (2019), 2205–2216. [8](#), [9](#)
- [7] Blom, F., Bouwstra, S., Elwenspoek, M., and Fluitman, J. Dependence of the quality factor of micromachined silicon beam resonators on pressure and geometry. *Journal of Vacuum Science & Technology B: Microelectronics and Nanometer Structures Processing, Measurement, and Phenomena* 10, 1 (1992), 19–26. [17](#)
- [8] Ceylan, S., Clinton, J. F., Giardini, D., Böse, M., Charalambous, C., Van Driel, M., Horleston, A., Kawamura, T., Khan, A., Orhand-Mainsant, G., et al. Companion guide to the marsquake catalog from insight, sols 0–478: Data content and non-seismic events. *Physics of the Earth and Planetary Interiors* 310 (2021), 106597. [6](#)
- [9] Clinton, J. F., Ceylan, S., van Driel, M., Giardini, D., Stähler, S. C., Böse, M., Charalambous, C., Dahmen, N. L., Horleston, A., Kawamura, T., et al. The marsquake catalogue from insight, sols 0–478. *Physics of the Earth and Planetary Interiors* 310 (2021), 106595. [4](#)

- [10] Da Silva, J. Optical Micro-Seismometer Based on Evanescent Field Perturbation of Whispering Gallery Modes. Master's thesis, Southern Methodist University, 2018. [15](#)
- [11] De Vos, K. *Label-free Silicon Photonics Biosensor Platform with Microring Resonators*. PhD thesis, Ghent University, 2010. [58](#)
- [12] Denu, G. A., Fu, J., Liu, Z., Mirani, J. H., and Wang, H. Effect of thermoelastic damping on silicon, gaas, diamond and sic micromechanical resonators. *AIP Advances* 7, 5 (2017), 055014. [16](#)
- [13] Du, X., Vincent, S., and Lu, T. Full-vectorial whispering-gallery-mode cavity analysis. *Optics express* 21, 19 (2013), 22012–22022. [35](#)
- [14] Fourquette, D., Otugen, M., Larocque, L., Ritter, G., Meeusen, J., and Ioppolo, T. Whispering-Gallery-Mode-Based Seismometer. July 3 2014. US Patent No. 8,743,372. [8](#)
- [15] Fourquette, D., Ötügen, V., Larocque, L., Ayaz, U., and Ritter, G. Optical MEMS-Based Seismometer. In *Proceedings of the 2012 Monitoring Research Review* (Albuquerque, NM, 2012). [9](#)
- [16] Guan, G., Arnold, S., and Otugen, V. Temperature Measurements Using a Microoptical Sensor Based on Whispering Gallery Modes. *AIAA Journal* 44, 10 (Oct 2006), 2385–2389. [10](#), [11](#)
- [17] He, L., Özdemir, Ş. K., Zhu, J., Kim, W., and Yang, L. Detecting single viruses and nanoparticles using whispering gallery microlasers. *Nature nanotechnology* 6, 7 (2011), 428–432. [12](#)
- [18] Hosaka, H., Itao, K., and Kuroda, S. Damping characteristics of beam-shaped micro-oscillators. *Sensors and Actuators A: Physical* 49, 1-2 (1995), 87–95. [16](#)
- [19] Huang, G., Lucas, E., Liu, J., Raja, A. S., Lihachev, G., Gorodetsky, M. L., Engelsens, N. J., and Kippenberg, T. J. Thermorefractive noise in silicon-nitride microresonators. *Physical Review A* 99, 6 (2019), 061801. [39](#), [45](#)
- [20] Huffman, T. A., Brodnik, G. M., Pinho, C., Gundavarapu, S., Baney, D., and Blumenthal, D. J. Integrated resonators in an ultralow loss  $\text{Si}_3\text{N}_4/\text{SiO}_2$  platform for multifunction applications. *IEEE Journal of selected topics in quantum electronics* 24, 4 (2018), 1–9. [59](#)
- [21] Hurley, J., Murdoch, N., Teanby, N., Bowles, N., Warren, T., Calcutt, S., Mimoun, D., and Pike, W. Isolation of seismic signal from insight/seis-sp microseismometer measurements. *Space Science Reviews* 214 (2018), 1–22. [7](#)
- [22] Inman, D. *Engineering Vibration*. Pearson, 2014. [25](#)
- [23] Ioppolo, T., Ayaz, U., and Ötügen, M. V. Tuning of Whispering Gallery Modes of Spherical Resonators Using an External Electric Field. *Opt. Express* 17, 19 (Sep 2009), 16465–16479. [11](#), [38](#)

- [24] Ioppolo, T., Ayaz, U. K., and Ötügen, M. V. High-Resolution Force Sensor Based on Morphology Dependent Optical Resonances of Polymeric Spheres. *Journal of Applied Physics* 105, 1 (2009), 013535. [10](#), [11](#)
- [25] Ioppolo, T., Das, N., and Ötügen, M. V. Whispering gallery modes of microspheres in the presence of a changing surrounding medium: A new ray-tracing analysis and sensor experiment. *Journal of Applied Physics* 107, 10 (2010), 103105. [11](#), [12](#), [34](#)
- [26] Ioppolo, T., Kozhevnikov, M., Stepaniuk, V., Ötügen, M. V., and Sheverev, V. Micro-optical Force Sensor Concept Based on Whispering Gallery Mode Resonators. *Appl. Opt.* 47, 16 (Jun 2008), 3009–3014. [10](#), [11](#), [22](#), [38](#)
- [27] Ioppolo, T., and Manzo, M. Dome-Shaped Whispering Gallery Mode Laser For Remote Wall Temperature Sensing. *Appl. Opt.* 53, 22 (Aug 2014), 5065–5069. [11](#)
- [28] Ioppolo, T., and Ötügen, M. V. Pressure Tuning of Whispering Gallery Mode Resonators. *J. Opt. Soc. Am. B* 24, 10 (Oct 2007), 2721–2726. [10](#), [11](#)
- [29] Ioppolo, T., and Ötügen, M. V. Magnetorheological Polydimethylsiloxane Micro-Optical Resonator. *Opt. Lett.* 35, 12 (Jun 2010), 2037–2039. [11](#), [12](#), [38](#)
- [30] Ioppolo, T., Ötügen, M. V., and Marcis, K. Magnetic Field-Induced Excitation and Optical Detection of Mechanical Modes of Microspheres. *Journal of Applied Physics* 107, 12 (2010), 123115. [11](#), [12](#)
- [31] Ioppolo, T., Ötügen, V., Fourquette, D., and Larocque, L. Effect of Acceleration on the Morphology-Dependent Optical Resonances of Spherical Resonators. *J. Opt. Soc. Am. B* 28, 2 (Feb 2011), 225–227. [10](#), [11](#), [12](#), [38](#)
- [32] Ioppolo, T., Stubblefield, J., and Ötügen, M. V. Electric Field-Induced Deformation of Polydimethylsiloxane Polymers. *Journal of Applied Physics* 112, 4 (2012), 044906. [11](#)
- [33] Laine, J.-P., Tapalian, C., Little, B., and Haus, H. Acceleration sensor based on high-q optical microsphere resonator and pedestal antiresonant reflecting waveguide coupler. *Sensors and Actuators A: Physical* 93, 1 (2001), 1–7. [11](#)
- [34] Lifshitz, R., and Roukes, M. L. Thermoelastic damping in micro-and nanomechanical systems. *Physical review B* 61, 8 (2000), 5600. [16](#)
- [35] Lim, J., Savchenkov, A. A., Dale, E., Liang, W., Eliyahu, D., Ilchenko, V., Matsko, A. B., Maleki, L., and Wong, C. W. Chasing the thermodynamical noise limit in whispering-gallery-mode resonators for ultrastable laser frequency stabilization. *Nature communications* 8, 1 (2017), 8. [48](#)
- [36] Lindsay, H. Alsep, apollo-lunar surface experiments package, 19 november 1969-30 september 1977. *Apollo Lunar Surface Journal* (2010). [vii](#), [2](#), [3](#)

- [37] Lognonné, P., and Johnson, C. 10.03 - planetary seismology. In *Treatise on Geophysics*, G. Schubert, Ed. Elsevier, Amsterdam, 2007, pp. 69–122. [2](#)
- [38] Lognonné, P., Banerdt, W. B., Giardini, D., Pike, W. T., Christensen, U., Laudet, P., De Raucourt, S., Zweifel, P., Calcutt, S., Bierwirth, M., et al. Seis: Insight’s seismic experiment for internal structure of mars. *Space Science Reviews* 215 (2019), 1–170. [2](#), [6](#)
- [39] Mansour, G., Tsongas, K., and Tzetzis, D. Investigation of the dynamic mechanical properties of epoxy resins modified with elastomers. *Composites Part B: Engineering* 94 (2016), 152–159. [17](#)
- [40] Manzo, M., Ioppolo, T., Ayaz, U. K., LaPenna, V., and Ötügen, M. V. A Photonic Wall Pressure Sensor for Fluid Mechanics Applications. *Review of Scientific Instruments* 83, 10 (2012), 105003. [11](#)
- [41] Mehrabani, S., Kwong, P., Gupta, M., and Armani, A. M. Hybrid microcavity humidity sensor. *Applied Physics Letters* 102, 24 (2013), 241101. [34](#)
- [42] Naeli, K., and Brand, O. Dimensional considerations in achieving large quality factors for resonant silicon cantilevers in air. *Journal of applied Physics* 105, 1 (2009), 014908. [16](#)
- [43] Namazu, T., Isono, Y., and Tanaka, T. Evaluation of size effect on mechanical properties of single crystal silicon by nanoscale bending test using afm. *Journal of Microelectromechanical systems* 9, 4 (2000), 450–459. [27](#)
- [44] Ötügen, M. V., Su, W.-J., and Papadopoulos, G. A new laser-based method for strain rate and vorticity measurements. *Measurement Science and Technology* 9, 2 (1998), 267. [49](#)
- [45] Park, S., and Gao, X. Bernoulli–euler beam model based on a modified couple stress theory. *Journal of Micromechanics and Microengineering* 16, 11 (2006), 2355. [14](#), [23](#)
- [46] R. Ali, A., Ioppolo, T., Ötügen, V., Christensen, M., and MacFarlane, D. Photonic Electric Field Sensor Based on Polymeric Microspheres. *Journal of Polymer Science Part B: Polymer Physics* 52, 3 (2013), 276–279. [11](#), [12](#)
- [47] Rayleigh, L. Cxii. the problem of the whispering gallery. *The London, Edinburgh, and Dublin Philosophical Magazine and Journal of Science* 20, 120 (1910), 1001–1004. [10](#)
- [48] Rubino, E., and Ioppolo, T. Young’s modulus and loss tangent measurement of polydimethylsiloxane using an optical lever. *Journal of Polymer Science Part B: Polymer Physics* 54, 7 (2016), 747–751. [28](#)
- [49] Salameh, E. R. *Optical Microresonator-Based Flow-Speed Sensor*. PhD thesis, Southern Methodist University, 2022. [51](#)

- [50] Salameh, E. R., Wise, A. K., da Silva, J., Volkan Ötügen, M., and Fourguette, D. Flow speed sensor based on optical microresonators. *AIAA Journal* 60, 5 (2022), 2953–2960. 9, 27, 48
- [51] Savchenkov, A. A., Matsko, A. B., Ilchenko, V. S., Yu, N., and Maleki, L. Whispering-gallery-mode resonators as frequency references. ii. stabilization. *JOSA B* 24, 12 (2007), 2988–2997. 48
- [52] Schurz, D. Easep press backgrounder. vii, 3
- [53] Soroka, W. W. Note on the relations between viscous and structural damping coefficients. *Journal of the Aeronautical Sciences* 16, 7 (1949), 409–410. 28
- [54] Sumali, H., and Carne, T. G. Air-drag damping on micro-cantilever beams. Tech. rep., Sandia National Lab.(SNL-NM), Albuquerque, NM (United States), 2008. 16, 29
- [55] Vollmer, F., Braun, D., Libchaber, A., Khoshsim, M., Teraoka, I., and Arnold, S. Protein detection by optical shift of a resonant microcavity. *Applied physics letters* 80, 21 (2002), 4057–4059. 34
- [56] Wielandt, E. Seismic sensors and their calibration. In *New Manual of Seismological Observatory Practice 2 (NMSOP-2)*. Deutsches GeoForschungsZentrum GFZ, 2012, pp. 1–51. 23
- [57] Wielandt, E., and Streckeisen, G. The leaf-spring seismometer: Design and performance. *Bulletin of the Seismological Society of America* 72, 6A (1982), 2349–2367. 7
- [58] Wielandt, Erhard. Design Considerations for Broadband Seismometers. <http://ds.iris.edu/stations/seisWorkshop04/PDF/Wielandt-Design3.pdf>, 2004. Note: This is an electronic document. Date of publication: [Date unavailable]; Date retrieved: August 31, 2018;. Date last modified: April 28, 2004. 7
- [59] Wise, B. A Microresonator-Based Laser Doppler Velocity Sensor For Interplanetary Atmospheric Re-Entry. Master’s thesis, Southern Methodist University, 2018. 12
- [60] Wise, B. J., Eghbalifarkoosh, V., Otugen, V., and Fourguette, D. A microresonator based laser velocity sensor. In *2018 AIAA Aerospace Sciences Meeting* (2018), p. 1770. 48
- [61] Zumberge, M., Berger, J., Hatfield, W., and Wielandt, E. A three-component borehole optical seismic and geodetic sensor. *Bulletin of the Seismological Society of America* 108, 4 (2018), 2022–2031. 8, 32
- [62] Zumberge, M., Berger, J., Otero, J., and Wielandt, E. An optical seismometer without force feedback. *Bulletin of the seismological society of America* 100, 2 (2010), 598–605. 7, 8
- [63] Zumberge, M., Berger, J., and Wielandt, E. Experiments with an optical seismometer. In *AGU Fall Meeting Abstracts* (2003), vol. 2003, pp. S52C–0144. 8